Atmos. Meas. Tech., 9, 553–576, 2016
www.atmos-meas-tech.net/9/553/2016/
doi:10.5194/amt-9-553-2016

Atmospheric Measurement Techniques
Open Access
EGU

A two-channel thermal dissociation cavity ring-down spectrometer for the detection of ambient NO_2, RO_2NO_2 and $RONO_2$

J. Thieser[1], G. Schuster[1], J. Schuladen[1], G. J. Phillips[1,a], A. Reiffs[1], U. Parchatka[1], D. Pöhler[2], J. Lelieveld[1], and J. N. Crowley[1]

[1]Max-Planck-Institut für Chemie, Division of Atmospheric Chemistry, Mainz, Germany
[2]Institute of Environmental Physics, University of Heidelberg, Heidelberg, Germany
[a]now at: Department of Natural Sciences, University of Chester, Chester, UK

Correspondence to: J. N. Crowley (john.crowley@mpic.de)

Received: 23 September 2015 – Published in Atmos. Meas. Tech. Discuss.: 3 November 2015
Revised: 4 January 2016 – Accepted: 28 January 2016 – Published: 17 February 2016

Abstract. We describe a thermal dissociation cavity ring-down spectrometer (TD-CRDS) for measurement of ambient NO_2, total peroxy nitrates (ΣPNs) and total alkyl nitrates (ΣANs). The spectrometer has two separate cavities operating at $\sim$405.2 and 408.5 nm. One cavity (reference) samples NO_2 continuously from an inlet at ambient temperature, the other samples sequentially from an inlet at 473 K in which PNs are converted to NO_2 or from an inlet at 723 K in which both PNs and ANs are converted to NO_2, difference signals being used to derive mixing ratios of ΣPNs and ΣANs. We describe an extensive set of laboratory experiments and numerical simulations to characterise the fate of organic radicals in the hot inlets and cavity and derive correction factors to account for the bias resulting from the interaction of peroxy radicals with ambient NO and NO_2. Finally, we present the first measurements and comparison with other instruments during a field campaign, outline the limitations of the present instrument and provide an outlook for future improvements.

1 Introduction

Reactive nitrogen oxides are centrally important trace gases in atmospheric chemistry as they affect air quality, climate and ecosystem nutrients. Nitrogen oxides are involved in the photochemical production/loss of ozone (O_3); they interact with RO_x radicals ($RO_x \equiv OH + HO_2 + RO_2$, where R is an organic fragment) to either catalyse ozone formation or terminate the HO_x catalytic chain and thereby suppress ozone formation. Nitrogen oxides are largely emitted to the atmosphere as NO which is then oxidised to NO_2. Beside inorganic NO_x ($NO_x \equiv NO + NO_2$) there are several classes of organic nitrogen oxides including peroxy nitrates (RO_2NO_2) and alkyl nitrates ($RONO_2$) which have an important influence on atmospheric composition. Peroxy nitrates and alkyl nitrates are produced as by-products in the photochemical oxidation of volatile organic compounds (VOCs) in the presence of NO_x, the same processes and reactions that produce the pollutant and greenhouse gas ozone. In addition to being indicators of photochemical ozone production, organic nitrates exert a direct influence on regional ozone levels and can have a large impact on the global distribution of NO_x and thus ozone (Singh and Hanst, 1981; Roberts, 1990).

Peroxy nitrates are formed in the reaction of RO_2 with NO_2 (Reaction R1) and their lifetime with respect to thermal decomposition (Reaction R2) is strongly temperature-dependent.

$$RO_2 + NO_2 + M \rightarrow RO_2NO_2 + M \quad \text{(R1)}$$
$$RO_2NO_2 + M \rightarrow RO_2 + NO_2 + M \quad \text{(R2)}$$

Peroxy nitrates such as peroxyacetic nitric anhydride (PAN, $CH_3C(O)O_2NO_2$), which possess an acyl group adjacent to the peroxy group, have thermal decomposition lifetimes that vary from less than an hour at the surface at temperatures close to 295 K, to more than a month at the low temperature of e.g. the upper troposphere. Consequently, peroxyacetic nitric anhydrides are important reservoirs of NO_x and mediators of its long-range transport to remote regions. In contrast, peroxy nitrates that do not possess the acyl group (e.g.

HO_2NO_2 or $CH_3O_2NO_2$) are much shorter lived and are only found in significant abundance in cold regions of the troposphere such as in the Antarctic boundary layer (Slusher et al., 2002) and the upper troposphere (Murphy et al., 2004; Kim et al., 2007; Browne et al., 2011; Nault et al., 2015). In the lowermost troposphere, other losses of RO_2NO_2 such as photolysis or reaction with OH are vastly reduced in importance compared to thermal decomposition (Talukdar et al., 1995). Throughout this paper, we use the term "PN" to refer to peroxy nitrates.

During daytime, alkyl nitrates ($RONO_2$) are formed in a minor branch of the reaction between organic peroxy radicals (RO_2) and NO (Reaction R3). The dominant reaction channel (Reaction R4) leads to the formation of NO_2 and therefore (via its photolysis) to ozone.

$$RO_2 + NO + M \rightarrow RONO_2 + M \quad \text{(R3)}$$

$$RO_2 + NO \rightarrow RO + NO_2 \quad \text{(R4)}$$

The fractional flux through Reaction (R3) (relative to Reactions R3 and R4) depends on the carbon chain and also the pressure and temperature and can vary from very low values (< 2 %) for small hydrocarbons to > 50 % for longer chain hydrocarbons such as heptane (Lee et al., 2014).

Alkyl nitrates can also be formed at night in the NO_3-induced degradation of unsaturated VOCs, which proceeds via addition of NO_3 across the double bond to form (in the presence of O_2) a nitrooxyalkyl peroxy radical that can further react to form an alkyl nitrate with e.g. hydroxyl or carbonyl groups:

$$NO_3 + R = R(+O_2) \rightarrow R'RONO_2. \quad \text{(R5)}$$

Yields of alkyl nitrates from these reactions can be large, especially for biogenic organics such as isoprene or terpenes (Atkinson and Arey, 2003). Hereafter, we use the term "AN" to refer to alkyl nitrates, irrespective of their mode of generation.

ANs which do not contain double bonds or hydroxyl groups generally have a low affinity for surfaces and react only slowly with oxidants such as OH (Talukdar et al., 1997) so that they can sequester a significant fraction of reactive nitrogen (Perring et al., 2013).

The organic nitrate content of ambient air comprises a mixture of many structurally distinct compounds in generally low individual abundance, which makes their quantitative determination challenging. Organic nitrates have been measured on many occasions using gas chromatography. The advantage of this technique is a limit of detection of a few parts per trillion volume (pptv) and the possibility to distinguish between individual organic nitrates (see e.g. Roberts et al., 2003). The disadvantages are the requirement of calibration for many trace gases (usually not commercially available) and low time resolution (Hao et al., 1994; Flocke et al., 2005). Recently, PAN and other peroxycarboxylic nitric anhydrides such as MPAN (peroxymethacrylic nitric anhydride) and PPN (peroxypropionic nitric anhydride) have been identified and measured with sub-second time resolution using thermal dissociation chemical ionisation mass spectrometry (TD-CIMS) (Slusher et al., 2004; LaFranchi et al., 2009; Wolfe et al., 2009; Roiger et al., 2011; Zheng et al., 2011; Mielke and Osthoff, 2012; Phillips et al., 2013).

The first measurements of alkyl nitrates in the atmosphere were made by Atlas et al. (1988), and subsequent calculations and measurements suggested that the atmosphere should contain a wide suite of individual alkyl and multifunctional nitrates (Calvert and Madronich, 1987; Atherton and Penner, 1988; Schneider and Ballschmiter, 1999) and that hydroxy alkyl nitrates derived from isoprene oxidation could constitute as much as 12–26 % of tropospheric NO_y (Trainer et al., 1991). Recent measurement of speciated ANs by chemical ionisation mass spectrometry (Beaver et al., 2012) has shown that biogenic derived ANs may represent a substantial fraction of the total AN mixture.

Total measured NO_y has frequently been found to exceed the sums of different nitrogen compounds ($NO + NO_2 + PAN + HNO_3 + HONO + NO_3 + 2N_2O_5 + \ldots$), the range of the "missing" NO_y being 10–20 %. In most of these observations the total alkyl nitrate content was not measured or only partially (e.g. Fahey et al., 1986; Buhr et al., 1990; Ridley et al., 1990; Parrish and Buhr, 1993; Singh et al., 1996; Williams et al., 1997). These considerations led to the development of instruments (Day et al., 2002) which make use of the thermal instability of RO_2NO_2 and $RONO_2$ at elevated temperatures and which report measurements of the sum of peroxy nitrates (ΣPN) or the sum of alkyl nitrates (ΣAN) by monitoring the NO_2 product of the thermal decomposition of PNs and ANs at different temperatures.

$$RO_2NO_2 \rightarrow RO_2 + NO_2 (> 420\,K) \quad \text{(R6)}$$

$$RONO_2 \rightarrow RO + NO_2 (> 630\,K) \quad \text{(R7)}$$

These studies have helped to confirm that ANs and PNs represent a significant fraction of atmospheric NO_y and confirm their role in e.g. HO_x radical chain termination, or as indicators of photochemical O_3 generation (see e.g. Day et al., 2003; Rosen et al., 2004; Perring et al., 2013).

Here we describe a recently constructed TD-CRD instrument to measure ambient NO_2 and also that formed from the thermal decomposition of ANs and PNs via cavity ring-down spectroscopy. Our instrument operates under similar conditions of pressure flow, oven temperature and laser wavelength to those described in Paul et al. (2009) and Paul and Osthoff (2010).

2 Principal of Operation and Instrument set-up

Cavity ring-down spectroscopy (hereafter CRDS) and its use for the sensitive detection of atmospheric trace gases has

been reviewed in detail (Berden et al., 2000; Brown, 2003). CRDS is based on direct absorption spectroscopy in which the absorption path length is enhanced by a high finesse cavity formed by a set of two highly reflective mirrors. Most applications use pulsed or intensity-modulated continuous-wave (CW) lasers as a light source with direct coupling into the cavity via one (front) mirror. The present experiment uses a square-wave, on/off-modulated CW laser. During the "laser on" phase the light intensity in the cavity builds up to a level determined by mirror reflectivity and transmission. The light leaking out through the back mirror during "laser off" mode is analysed to derive an exponential decay constant, which is reduced in the presence of an absorbing or scattering gas. This provides an absolute measurement of optical extinction, as given in Eq. (1).

$$\sigma[A] = \alpha = \frac{l}{cd}\left(\frac{1}{\tau} - \frac{1}{\tau_0}\right), \quad (1)$$

where σ is the absorption cross section of the absorber, averaged over the laser spectrum, $[A]$ is the concentration of the absorber, α is the optical extinction coefficient (units of inverse length), c is the speed of light, τ and τ_0 are the exponential decay constants with and without the absorber in the cavity and l/d is the ratio of the length over which the absorber is present to the distance between the two resonator mirrors. In order to derive τ_0 the cavity is flushed with zero air (see Sect. 2.1.1).

Essential features of the TD-CRDS instrument described here are displayed in Fig. 1. Our two-channel CRDS utilises two laser diodes (Laser Components, optical power: 120 mW) in commercially available laser diode heads (Thorlabs) with current and temperature controller units (Thorlabs ITC 510 and ITC 502). The use of two lasers rather than one increases the light intensity at the detector and thus improves the signal-to-noise ratio, but brings with it the added complexity of needing to measure two-laser spectra (see below) and using two different NO_2 absorption cross sections.

The lasers are modulated on and off at 1666 Hz (duty cycle 50 %) by a 6 V square-wave signal. The rise and fall time of the intensity is less than 1 µs, which, under normal conditions (NO_2 < 1 ppm), is rapid on the timescale of the decay of intensity from the optical cavities. Optical isolators (consisting of a linear polariser and a quarter-wave plate) are used to prevent back reflections from the front mirror from entering the lasers. The laser diodes are stabilised at about 40 °C and about 50 °C resulting in wavelengths centred at about 405.2 and 408.5 nm, respectively. The laser emission is monitored at regular intervals by coupling weak specular reflection from either of the front mirrors via an optical fibre into a spectrometer (∼ 0.1 nm resolution, OMT, temperature-regulated CCD detector with 3648 pixels). Small variations in the laser wavelength are observed (peak-to-peak variability of < 2 % over consecutive, 10 min averaging intervals), which result in the same variability of the effective absorption cross section. Figure 2 shows the laser emission spectra (blue and red) along with the NO_2 absorption spectrum (black line, right y axis, (Voigt et al., 2002). The relatively broad laser emission ensures the passive mode matches with resonant frequencies of the cavity, avoiding the need for active mode-matching (Ayers et al., 2005). Effective absorption cross sections were obtained by multiplying the normalised laser emission spectra by the structured absorption of NO_2.

The cavity mirrors (1 inch diameter, 1 m radius of curvature) have a nominal reflectivity of 0.999965 (Advanced Thin Films). The mirrors are mounted in a self-made mirror holder system, the ∼ 70 cm distance between them being rigidly fixed using three hollow carbon fibre rods (outer diameter 15 mm) per cavity. This combination of mirror reflectivity and separation results in ring-down times under typical conditions (830 mbar air) of about τ_0 =38 µs when no absorber is present, or optical path lengths of > 10 km. A purge flow, 100 cm^3 (STP) min^{-1} (hereafter sccm), of zero air protects each mirror from contamination by ambient air and subsequent loss of reflectivity.

The light transmitted through the back mirror of the cavity is detected by a photomultiplier, located behind a lens and an interference filter (10 nm full width at half maximum height centred at 405 nm) to reject stray light. The preamplified signal is digitised by a USB digital oscilloscope (PicoScope 3000, 12 bit vertical resolution, 5 Mhz sampling rate), with 1344 ring-down traces being averaged in order to achieve the desired signal-to-noise ratio. This number results from minimising read-out time from the PicoScope by measuring sequential 42 ring-down traces (filling internal memory) before reading out the data. This cycle is repeated 32 times, resulting in a time resolution of about 4 s per data point for both channels.

The two-channel CRDS consists of two nominally identical cavities (both thermostatted to 308 K) and sample inlets. The cavities are made of 10 mm inner diameter Duran glass, which was coated with a thin film of Teflon (DuPont, FEP TE9568) to minimise interaction of traces gases with the walls, which could potentially result in loss or production of NO_2. Aerosols are prevented from entering the inlets and cavities using a 47 mm diameter, 2 µm PTFE filter (PAL Teflon).

The cavities are operated at sub-ambient pressure (typically 800–850 mbar) which is held constant using an additional, mass-flow-controlled branch, linking the inlet manifold to a pump. This line also contains a relative humidity and temperature sensor to enable corrections for laser light scattering by H_2O vapour to be made (see Sect. 2.1.3). Ambient air enters the centre of the cavities at a flow rate of 2.0 L min^{-1} (STP) in each channel, resulting in a cavity residence time of about 1.2 s. However, as concentrations are integrated over the entire cavity length, the average residence time of a molecule of detected in the cavity will be less than this.

Values of τ_0 were obtained at regular intervals (every 5–10 min) by switching ambient air for zero air for a short pe-

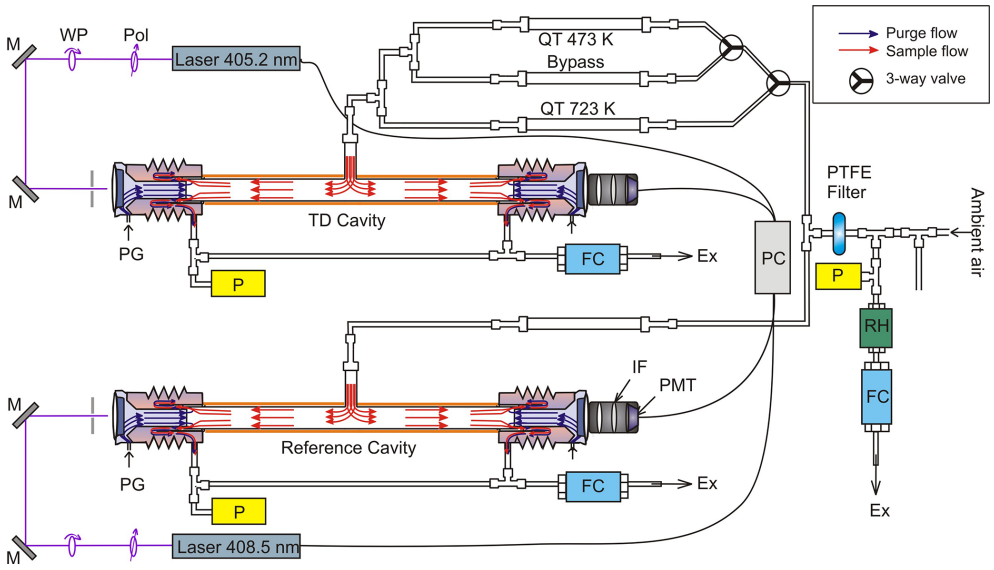

Figure 1. Schematic diagram of the two cavities (reference and TD) and associated inlets (quartz tubes at ambient temperature, 473 or 723 K). The reference cavity samples continuously via a quartz tube at ambient temperature, the TD cavity samples sequentially from quartz tubing at ambient temperature, 473 or 723 K. Both cavities are held at 308 K and at constant pressure (usually 800 mbar). M: mirror, WP: quarter-wave plate, Pol: polariser, QT: quartz tubing, P: pressure transducer, FC: mass flow controller, PC: computer, RH: relative humidity and temperature sensor, IF: interference filter, PMT: photomultiplier, PG: purge gas, Ex: exhaust.

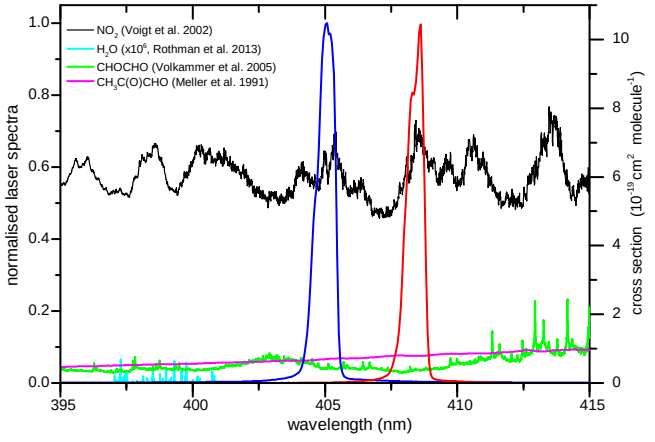

Figure 2. Laser emission spectrum (left y axis) measured in the reference cavity (blue) and the TD cavity (red). The absorption spectra (Meller et al., 1991; Voigt et al., 2002; Volkamer et al., 2005b; Rothman et al., 2013) are associated with the right y axis. The H_2O spectrum is scaled by a factor of 1×10^6.

riod (1–2 min). Three-way Teflon valves (NResearch) which have been shown not to permanently remove PNs, ANs or NO_2 were used. This frequency of zeroing was found to be sufficient to track drifts in the ring-down constant (see later).

One of the cavities (reference cavity in Fig. 1) continuously measures ambient NO_2; the second cavity (TD cavity) samples alternatively from three separate, quartz tubes of i.d. 1.5 cm and length 42 cm. Fifteen centimetre sections of two of the quartz tubes were placed in commercial ovens (Carbolite) and heated up to 473 and 723 K, whereby these are oven temperatures and do not necessarily reflect the temperature of gas flowing through the quartz tubing. The cavity attached to the heated quartz inlets thus measures the sum of NO_2 plus NO_2 generated from the thermal dissociation of organic nitrates. We refer to the NO_2 measurements when sampling from these inlets as $[NO_2]_{ref}$, $[NO_2]_{TD}$, $[NO_2]_{TD\ 473}$ and $[NO_2]_{TD\ 723}$.

The strength of the NO_2 bond within the parent compound defines the temperature at which thermal dissociation (to form NO_2) is feasible. The ROO–NO_2 bond strengths for peroxy nitrates lie between ~ 85 and 115 kJ mol^{-1} (Kirchner et al., 1999) which is significantly weaker than the RO–NO_2 bond strength for alkyl nitrates (160–170 kJ mol^{-1}, Roberts, 1990). For comparison, the HO–NO_2 bond strength for nitric acid is ~ 200 kJ mol^{-1} (Atkinson et al., 2004). As discussed by Day et al. (2002) efficient thermal dissociation to NO_2 occurs at temperatures > 420 K for peroxy nitrates, > 630 K for alkyl nitrates and > 900 K for HNO_3. Based on purely thermodynamic considerations, and following Day et al. (2002), we do not expect to convert significant amounts of HNO_3 to NO_2 in either of our inlets. However, the recent data set of Wild et al. (2014) indicates that in their inlet at 723 K, substantial decomposition (~ 70 %) of HNO_3 to NO_2 takes place. As HNO_3 is a significant and highly variable fraction of boundary-layer NO_y, this may represent a potential artefact for our measurements of ambient ΣANs. In order to assess this, we conducted some experiments to check whether HNO_3 is detected as NO_2 in our TD 723 inlet. A simple HNO_3 permeation source was set up by passing a

small flow of air (≈ 20 sccm) through a metre of 1/16″ PFA tubing immersed in 66 % HNO_3 solution at room temperature and diluting this to ∼ 5 L (STP) min^{-1} (hereafter SLM) before adding the resultant flow directly to the inlets.

Figure S1 of the Supplement shows the efficiency of detection of HNO_3 as a function of oven temperature at a relative humidity (measured at 298 K) of 40 %. Assuming that we detect 100 % of HNO_3 at ∼ 950 K (about 2 ppbv) we can derive an efficiency of ∼ 10 % at the normal inlet temperature of 723 K, which is substantially less than the 70 % at 723 K reported by Wild et al. (2014). The reduction of NO_2 at $T > 900$ K is seen for additions of both HNO_3 and pure NO_2 and may reflect its surface catalysed decomposition at these elevated temperatures. Based on this single measurement, ambient levels of 2 ppb for HNO_3 would result in a 0.2 ppb bias to the measurements of the ΣANs. However, the true size of a bias to the ambient measurements of ΣANs presented later is much smaller as HNO_3 transmission through the long (∼ 10 m), unheated, Teflon inlets and filter used is expected to be poor (Neuman et al., 1999). For the purpose of this paper we assume, as has been done in numerous previous studies (Day et al., 2002), that HNO_3 does not impact the measurements of our ΣANs significantly. Strictly speaking, in the absence of independent HNO_3 measurements, the ambient ΣANs mixing ratios we present later are thus to be regarded as upper limits. In a similar vein, we assume throughout that we have 100 % inlet transmission for all PNs and all ANs but recognise that some loss of "sticky" hydroxynitrates may occur.

The cavity which normally samples from the 473 or 723 K inlets can also be switched to sample at ambient temperature (via the "bypass" inlet shown in Fig. 1), enabling direct comparison of NO_2 measurements in the two cavities. As this method for detection of ΣANs and ΣPNs relies on the difference in NO_2 mixing ratios when sampling from the heated and unheated inlets, tests were carried out to establish that equal concentrations of NO_2 are measured in each cavity when only NO_2 is present. This data set, displayed as Fig. S2, yields slopes of unity when the TD cavity sampled NO_2 (2–80 ppb) from the 473 and 723 K inlets.

The residence time inside the heated quartz tubes and the connection tubing after splitting the air stream is about 2.5 s before reaching the cavities. The temperature profile inside the heated part of the quartz tube is non-uniform and the operating temperature was chosen to ensure complete dissociation of the organic nitrates. Figure 3 displays the relative NO_2 signals measured when ramping the temperature of the ovens from 323 to 803 K and passing dilute samples of either PAN, 2-propyl nitrate or *i*-butyl nitrate through the heated inlets. This shows clearly that the thermal decomposition of PAN is complete at oven temperatures greater than 443 K. For the two alkyl nitrates tested, very similar profiles are obtained, indicating that decomposition is negligible at temperatures < 493 K but that temperatures above ∼ 693 K are sufficient for complete decomposition to NO_2. These observations are consistent with those reported for similar TD setups to determine peroxy and alkyl nitrates (Day et al., 2002; Wooldridge et al., 2010; Zheng et al., 2011). Based on these results, the ovens were set to temperatures of 473 and 723 K (vertical lines in Fig. 3).

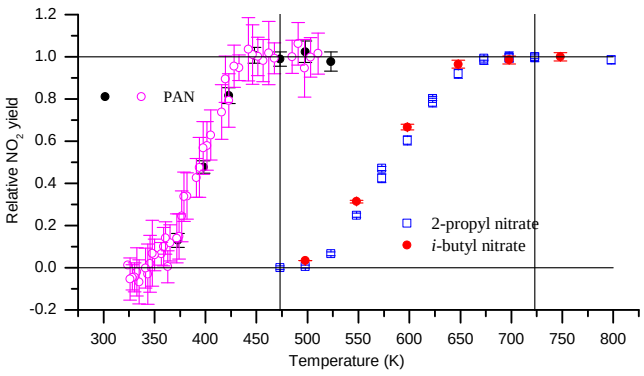

Figure 3. Efficiency of thermal dissociation of PAN and the ANs 2-propyl nitrate and *i*-butyl nitrate. PAN (≈ 500 pptv) was formed by the photolysis of acetone/NO/air sample (see text for details). The purple and black data points were measured before and after a campaign (≈ 2 months separation in time). The ANs were available as diluted samples (several parts per million by volume, ppmv) in air which were diluted to ≈ 10 ppbv for these tests. The vertical lines indicate the nominal oven temperatures finally used.

For initial estimates of the conversion efficiency of PNs and ANs to NO_2 we conducted tests using samples of PAN and 2-propyl nitrate of known concentration. For PAN we used a photochemical source (Phillips et al., 2013) in which NO is converted to PAN via a series of oxidation steps involving the photolysis of acetone in air. The PAN source is similar to those reported e.g. in Warneck and Zerbach (1992) and Flocke et al. (2005) who have shown that NO is converted with > 90 % efficiency to PAN. A plot of the NO_2 signal from the TD-CRDS vs. the calculated concentration of PAN (150 to 600 pptv) is given in Fig. S3. In this case, PAN was calculated by multiplying the NO mixing ratio (itself calculated from the manufacturer's specification and dilution factors) by 1.1. In this range of PAN mixing ratios, the response of the TD-CRDS to various NO (and thus PAN) concentrations is linear, with a gradient close to unity, initially suggesting that PAN detection as NO_2 is quantitative in our TD-CRDS.

Samples of alkyl nitrates in air of known concentrations (∼ 3 and ∼ 6 ppb) were prepared manometrically and used to derive the stoichiometry of conversion of 2-propyl nitrate to NO_2. The results are also displayed in Fig. S3 and indicate that at 723 K, 2-propyl nitrate in air is quantitatively converted to NO_2. Later we discuss the effects of non-stoichiometric conversion of PAN and ANs to NO_2 due to reactions of the organic radical fragment formed during thermal dissociation.

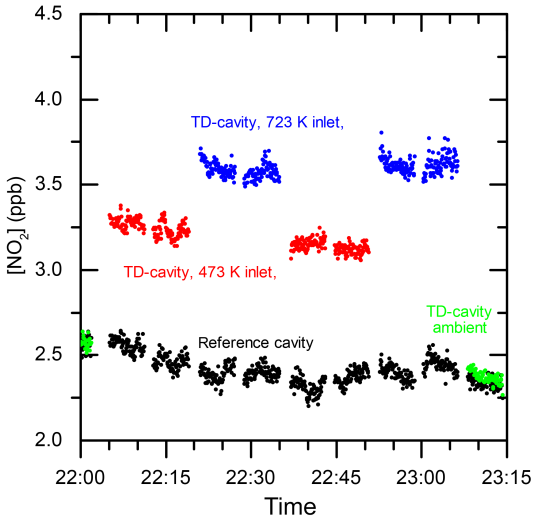

Figure 4. Example of a typical measurement cycle (showing raw data) when sampling ambient air. The black data points show the continuously measured NO_2 mixing ratios measured by the reference cavity. The green, red and blue data points were recorded in the TD cavity when sampling from the inlets at ambient temperature, 473 and 723 K, respectively.

A typical measurement sequence (in this case with an ambient air sample) is illustrated in Fig. 4 which displays NO_2 mixing ratios in both cavities. The black data points show NO_2 measurements in the reference cavity; the blue and red data points were obtained when the TD cavity sampled from the 723 and 473 K ovens, respectively. The green data points were obtained in the TD cavity when the gas was sampled via the bypass and serve as a check for consistency between the two cavities. The gaps in the data indicate zeroing periods when the inlet was filled with synthetic air. Zeroing was conducted at the same pressure as the measurement to avoid changes in ring-down due to changes in Rayleigh scattering by air. Note that the change in ring-down time at 405 nm caused by a 3.3 mbar change in pressure of air is the equivalent of $\sim$100 pptv of NO_2. As we discuss later, the use of dry zero air to derive τ_0 also requires correction for the difference in scattering cross section of dry and humid (i.e. ambient) air. Experiments to derive correction factors for this effect are described in Sect. 2.1.

Subtraction of the NO_2 mixing ratio measured when sampling from the reference cavity ($[NO_2]_{ref}$) from that obtained in the cavity sampling from the 473 K inlet ($[NO_2]_{473}$) in principal yields the summed mixing ratio of PNs that decompose thermally at this temperature. The main contributor will usually be $CH_3C(O)O_2NO_2$ (PAN), with contributions from larger PNs and other NO_2-containing trace gases (e.g. N_2O_5, see later) which also readily decompose at this temperature. In order to derive the ΣANs mixing ratio we first have to interpolate $[NO_2]_{TD\ 473}$ (red data points) and then subtract this from $[NO_2]_{TD\ 723}$ (blue data points). The need to interpolate the data from the 473 K channel means that the accuracy of the measurement of the ΣANs is impacted by variability of the mixing ratio of the ΣPNs.

2.1 Data corrections

2.1.1 *l* to *d* ratio

Owing to the use of purge gas flows at the mirrors, the physical distance between the mirrors (d) is longer than the length through which optical absorption takes place (l). The ratio of d to l was obtained by flowing a constant amount of NO_2/N_2 though the cavity and varying the purge gas flow from 0 to 500 sccm as shown previously for our red-laser instrument for measuring NO_3 and N_2O_5 (Schuster et al., 2009). The reduction in NO_2 signal at a purge gas flow of 100 sccm compared to when the complete volume between the mirrors was flushed with NO_2 (no mirror purge) was 5 %, indicating a d to l ratio of 1.06.

2.1.2 Inlet and filter loss of NO_2, PNs and ANs

The inlet transmission and filter losses were investigated in the laboratory for NO_2, ΣPNs and ΣANs. The response to concentration changes was nearly instantaneous, suggesting that wall losses or associated memory effects on the inlet and cavity tubing are insignificant. Transmission through a fresh PTFE filter (2 µm pore size) housed in a PFA filter holder was, within measurement precision, quantitative. Daily replacement when sampling ambient air was found to be sufficient to maintain this high transmission.

2.1.3 Relative humidity

Use of dry zero air to derive τ_0 requires correction for the fact that the Rayleigh scattering cross section of water vapour is smaller than that of dry air. The size of this effect was investigated in the laboratory by comparing τ_0 (obtained in dry zero air) to τ in zero air at various relative humidities (RHs) between 10 and 70 % (Delta Ohm, HD49T) at room temperature. The results are displayed in Fig. 5 which, at constant total pressure, shows a linear decrease in extinction with increasing water vapour concentration. This confirms that, in contrast to the conclusions of Hargrove and Zhang (2008) who found a large, positive interference caused by water vapour at 405 nm, the effect of H_2O in ambient air is to reduce extinction due to its lower Rayleigh scattering cross section. The slope of the fit in Fig. 5 yields a cross section difference between water vapour and dry air of $\Delta\sigma_{\text{Rayleigh}}^{405-409\,\text{nm}} = (-4.0 \pm 0.4) \times 10^{-27}\ \text{cm}^2\ \text{molecule}^{-1}$. This is somewhat lower than the value of $\Delta\sigma_{\text{Rayleigh}}^{405-409\,\text{nm}} = (-5.0 \pm 0.2) \times 10^{-27}\ \text{cm}^2\ \text{molecule}^{-1}$ obtained at 404 ± 0.5 nm by Fuchs et al. (2009). To put this in context, the correction applied for an ambient relative humidity of 70 % at 22 °C is equivalent to 130 pptv NO_2 under normal operating conditions. At low NO_2 mixing ra-

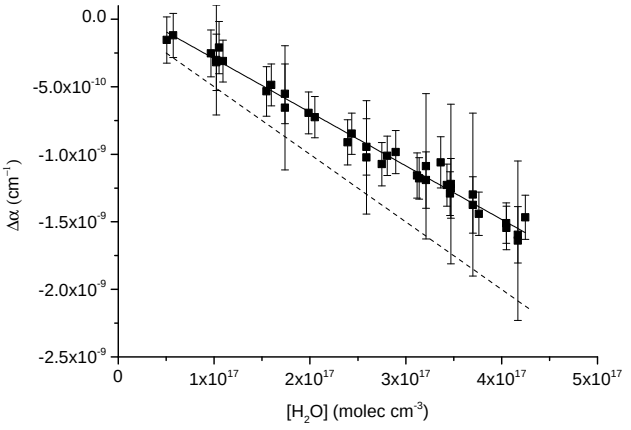

Figure 5. Determination of the scattering cross section of H_2O at 405 nm. $\Delta\alpha$ is the change in measured extinction when H_2O is added to dry air ($\Delta\alpha = \alpha(\mathrm{RH}=0) - \alpha(\mathrm{RH}>0)$). The dashed line is the calculated value of $\Delta\alpha$ when using the difference in scattering cross sections in dry and humid air reported by Fuchs et al. (2009).

tios the correction is therefore large (e.g. 100 % at 100 pptv). We discuss the impact of this later when assessing the total uncertainty.

2.1.4 Presence of NO_2 in zero air

The presence of NO_2 in the zero air used would lead to an underestimation of the ambient NO_2 concentrations. In order to check for NO_2 impurity in bottled zero air (hydrocarbon-free) we constructed and characterised an efficient, all-quartz blue-light converter (BLC) (Kley and McFarland, 1980) to remove NO_2. The BLC consisted of a thin (ID 10 mm) quartz tube of $\sim$ 30 cm length with the light from two LED arrays operating at a central wavelength of $\sim$ 390 nm coupled into the tube via quartz end windows. NO_2 entered and exited the BLC via side arms located close to the end windows and, at a flow rate of 1 SLM, was removed with an efficiency of $\sim$ 60 %, independent of NO_2 mixing ratios up to about 1 ppb. The use of quartz rather than Teflon for the construction of the BLC reduces memory effects related to NO_2 degassing from or being formed on UV-illuminated Teflon surfaces. The level of NO_2 in the zero air could thus be monitored with the CRDS by flowing the air through the BLC and modulating the light on and off over several 1 min cycles. In all bottles tested during a field campaign (PARADE; see Sect. 3) no change in NO_2 signal was observed, placing an upper limit of about 20 pptv of NO_2 in the zero air, implying a maximum bias of -20 pptv in the NO_2 measurements.

2.1.5 Formation of NO_2 via O_3 + NO

Common to several established instruments that measure NO_2, its formation in a dark reaction between NO and O_3 in e.g. an inlet line has to be considered (Ryerson et al., 2000).

$$\mathrm{NO} + \mathrm{O_3} \rightarrow \mathrm{NO_2} \qquad \text{(R8)}$$

Laboratory experiments were thus conducted to examine the formation of NO_2 via the reaction of O_3 with NO, in which mixing ratios of NO (0–10 ppbv) and O_3 (25, 48 or 80 ppbv) were varied systematically. NO was taken from a bottled standard, O_3 was formed by passing synthetic air over a Pen-Ray® lamp and its concentration was monitored using a photometric O_3 analyser (Thermo Environmental Instruments, model 49).

Under conditions of low conversion of NO and O_3, the amount of NO_2 formed $[NO_2]_t$ can be calculated from the initial concentrations of NO and O_3 and the reaction time (t): $[NO_2]_t = k_8[NO][O_3]t$, where k_8 is the rate coefficient for Reaction (R8) and is given as $2.07 \times 10^{-12} \exp(-1400/T)\,\mathrm{cm^3\,molecule^{-1}\,s^{-1}}$ (Atkinson et al., 2004) which results in a room temperature rate coefficient of about $1.9 \times 10^{-14}\,\mathrm{cm^3\,molecule^{-1}\,s^{-1}}$. For the NO_2 reference channel (inlet at 298 K, cavity at 308 K) the amount of NO_2 formed was entirely consistent with the kinetic parameters and reaction time used. This is demonstrated in Fig. 6 (upper panel).

The expression above indicates that the rate coefficient increases significantly with temperature so that an increase in the formation of NO_2 would be expected in the ovens of the TD cavity. Indeed, in order to explain the formation of NO_2 in the 473 and 723 K channels, "effective" rate coefficients of $k_{8\mathrm{eff}} = 2.5 \times 10^{-14}$ and $6.2 \times 10^{-14}\,\mathrm{cm^3\,molecule^{-1}\,s^{-1}}$, respectively were necessary. These effective rate coefficients are substantially lower than those derived from the parameterisation given above ($1.1 \times 10^{-13}\,\mathrm{cm^3\,molecule^{-1}\,s^{-1}}$ at 473 K and $3.0 \times 10^{-13}\,\mathrm{cm^3\,molecule^{-1}\,s^{-1}}$ at 723 K) and correspond to lower effective or average temperatures ($\sim$ 320 and 400 K, respectively) experienced by gas passing through the inlets and cavities. Numerical simulations of the reaction between NO and O_3 taking place in the oven and cavities were conducted using a measured temperature profile (see below). The amount of NO_2 formed in the simulation of Reaction (R8) was converted to an effective rate coefficient using the expression above. The result for the 723 K cavity was a value of $k_{8\mathrm{eff}} \sim (6.4 \pm 0.5) \times 10^{-14}\,\mathrm{cm^3\,molecule^{-1}\,s^{-1}}$ where the scatter in the retrieved effective rate constant was the result of simulations using different initial amounts of O_3. This is entirely consistent with the experimental observations.

The effective rate coefficients ($k_{8\mathrm{eff}}$) are thus appropriate for making corrections for NO_2 formed from O_3 + NO in this particular system. In order to illustrate the size of this correction, we assume $O_3 = 50$ ppb, NO = 1 ppb, $NO_2 = 5$ ppb, which are typical of a semi-polluted environment during daytime. The amount of NO_2 formed in the reference (cold) channel via this route is 0.1 ppbv or 2 % of ambient NO_2. This increases to 2.6 and 6.5 % in the 473 and 723 K channels, respectively.

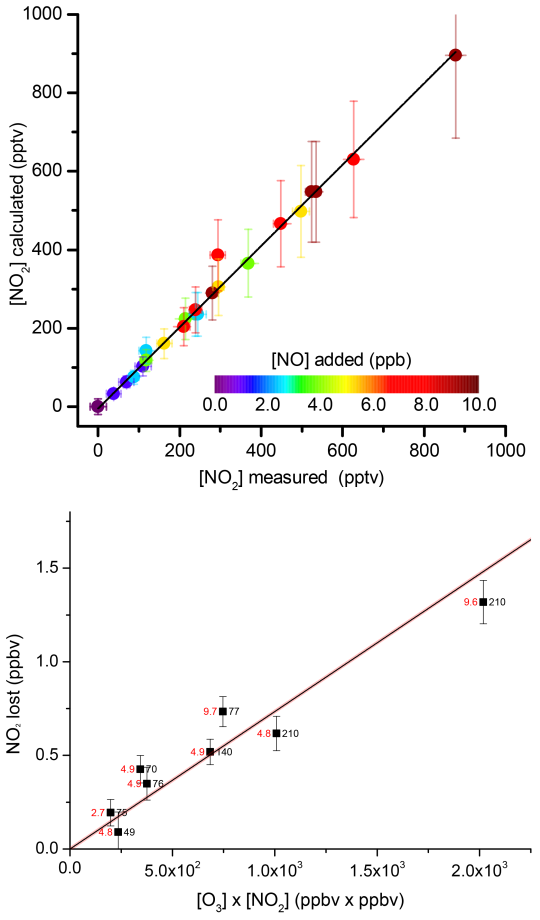

Figure 6. Upper panel: NO_2 formation in the reaction of O_3 (25, 48 or 80 ppbv) with NO in the inlet (in this case at ambient temperature), and reference cavity (at 308 K) and connecting tubing. The error bars on the calculated NO_2 formed are derived from the ∼ 20 % error in the rate coefficient given for the rate coefficient (Atkinson et al., 2004). The fit to the data (black line) yields a slope of 1.04 ± 0.08. Lower panel: loss of NO_2 as a result of the thermal decomposition of O_3 to O atoms and Reaction (R11). The black numbers to the right of each symbol indicate the O_3 mixing ratio (ppbv); the red numbers to the left represent the initial NO_2 amount (in ppbv). The straight black line is a weighted fit to the data with a slope of 7.34×10^{-4} ppbv^{-1}. The transparent red line is the NO_2 loss (in ppbv) calculated as described in the text with $[O]_{ss} = [O_3]/276$.

2.1.6 Pyrolysis of O_3

The potential for the reduction of NO_2 to NO via reaction with $O(^3P)$ atoms (henceforth O) formed in the thermal degradation of O_3 has been discussed by Day et al. (2002) who showed that it is of negligible importance for measurements of PNs and ANs at the temperatures of their heated inlets and their residence times. However, more recently, the same group has shown that at slightly higher oven temperatures, this effect may be significant (Lee et al., 2014). Peukert et al. (2013) have recently provided a parameterisation for the thermal decomposition rate coefficient of O_3 (k_9) that results in a value of 0.2 s^{-1} at 473 K, increasing to 520 s^{-1} at 723 K, the temperatures of the two ovens used here. The fate of O atoms formed is almost exclusively recombination with O_2 (with rate coefficient k_{10}).

$$O_3 \rightarrow O + O_2 \quad \text{(R9)}$$

$$O + O_2 + M \rightarrow O_3 + M \quad \text{(R10)}$$

This leads to a steady-state expression for the O atom concentration of $[O]_{ss} = k_9\ [O_3]/k_{10}\ [O_2]$. At 723 K, the forward and back reactions are both fast (several 100 s^{-1}) and a steady state is rapidly acquired. Thus at an ambient O_3 level of 50 ppbv, the O atom concentration in a steady state at 723 K would be 2.6×10^{11} atom cm^{-3}; i.e. O atoms represent a substantial fraction (> 20 %) of odd oxygen ($O + O_3$) at 723 K.

The lifetime for NO_2 loss with respect to reaction with O (Reaction R11) at 723 K is given by $(k_{11} \times [O])^{-1}$ and is equal to ∼ 0.6 s. Thus, the loss of NO_2 due to reaction with O from the thermal decomposition of O_3 depends sensitively on the residence time in the oven and on the temperature profile in the oven.

$$O + NO_2 \rightarrow NO + O_2 \quad \text{(R11)}$$

We have examined the impact of this reaction in laboratory experiments in which NO_2 (in varying amounts) was detected simultaneously in both the TD cavity with the oven at 473 or 723 K and the ambient temperature inlet/cavity whilst O_3 (also in varying amounts) was added. At 473 K no measurable effect was observed, which is consistent with the observations of Day et al. (2002) and a calculated O atom concentration of 2×10^7 atom cm^{-3}.

In contrast, at 723 K, a loss of NO_2 is indeed observed at high O_3 concentrations and the results are displayed in the lower panel of Fig. 6 where we plot the measured loss of NO_2 vs. the product of the NO_2 and O_3 mixing ratios. The individual NO_2 (red) and O_3 (black) mixing ratios (in ppbv) are listed to the left and right of the symbols.

The solid black line is a least squares fit to the data with the amount of NO_2 lost, L_{NO_2} (ppbv), given by

$$L_{NO_2} = 7.34 \times 10^{-4}[NO_2][O_3], \quad (2)$$

where the mixing ratios of O_3 and NO_2 are also given in ppbv.

The rationale for representing the data this way is that the loss rate of NO_2 is given by the expression $-d[NO_2]/dt = k_{11}[NO_2][O]_{ss}$, where $[O]_{ss}$ is proportional to $[O_3]$ (see above). k_{11} displays a weak temperature dependence, with recommended values of ∼ 6–8 × 10^{-12} cm^3 molecule^{-1} s^{-1} between 400 and 740 K (Atkinson et al., 2004). By taking an average contact time for transport through the ovens and cavity of 3 s (as in Sect. 2.1.5) and a value of

$k_{11} = 7 \times 10^{-12}$ cm^3 molecule^{-1} s^{-1}, we calculate the loss of NO_2 by adjusting the value of $[O]_{ss}$ / $[O_3]$ until agreement with the experimental results is observed. This procedure returns a value of $[O]_{ss} = [O_3]/276$ and is represented by the thick, transparent red line in Fig. 6. This effective ratio of [O] to $[O_3]$ is much smaller than that indicated above which is partly a result of using an average transport time through the oven and cavity and thus an average temperature, and partly via loss of O atoms (see below).

Equation (2) thus enables us to perform a simple correction to account for NO_2 loss though O_3 decomposition in the 723 K oven and TD cavity. The size of the correction depends sensitively on the O_3 concentration. For example, at $[O_3] = 50$ ppbv we calculate that from an initial NO_2 mixing ratio of 5 ppbv, we would lose 0.18 ppbv, i.e. less than 4 %.

To further our understanding of the processes involved, we have also conducted numerical simulations of a simple reaction scheme in which various amounts of O_3 and NO_2 pass through the hot oven and piping, and are thereby exposed to the temperature profile displayed in Fig. S4. The simulations, which included Reactions (R8)–(R11) and also the reaction of O with O_3, showed that at high O_3 levels, > 10 % of the NO_2 passing through the 723 K oven would be consumed by the reaction with O, clearly overestimating the measured effect. The results of the series of simulations are summarised in Fig. S5 which also shows the experimental data. Good agreement (green data points) is obtained when an extra loss term (e.g. wall loss) for the O atoms of ≈ 70 s^{-1} was incorporated in order to reduce their steady-state concentration. This is in accord with the observations of Day et al. (2002), who also invoked a loss of O atoms to account for observed NO_2 loss rates which were also much lower (factor of 4) than calculated. In our system, the predicted loss of NO_2 without O atom wall loss (purple symbols) is a factor of ~ 2 too large. This may be partially a result of loss of O atoms to walls, but may also be related to the fact that the pyrolysis rate constant for O_3 is highly temperature-dependent and a change in oven temperature from 723 K to e.g. 703 K would reduce the O atom concentration by a factor of ~ 1.5.

2.1.7 Reactions of organic radicals with NO and NO_2

The method of thermal dissociation of PNs or ANs to NO_2 and subsequent monitoring of NO_2 requires knowledge of the stoichiometry of the conversion factor under operating conditions. As discussed already (Day et al., 2002; Wooldridge et al., 2010), deviation from an ideal conversion factor of unity occurs when the NO_2 formed in the thermal dissociation recombines with the organic radical, or when the organic radical can react with other atmospheric substituents (such as NO) to form NO_2. The reactions which take place in the 473 and 723 K inlets are discussed below.

473 K inlet

Alkyl nitrates pass through the 473 K inlet without dissociation so we need only to consider the fate of PNs. For PAN ($CH_3C(O)O_2NO_2$) the major reactions that either form or consume NO_2 are

$$CH_3C(O)O_2NO_2 + M \rightarrow CH_3C(O)O_2 + NO_2 + M \quad \text{(R12)}$$
$$CH_3C(O)O_2 + NO_2 + M \rightarrow CH_3C(O)O_2NO_2 + M \quad \text{(R13)}$$
$$CH_3C(O)O_2 + NO(+O_2) \rightarrow NO_2 + CH_3O_2 + CO_2 \quad \text{(R14)}$$
$$CH_3O_2 + NO(+O_2) \rightarrow HCHO + HO_2 + NO_2. \quad \text{(R15)}$$
$$HO_2 + NO \rightarrow OH + NO_2 \quad \text{(R16)}$$
$$OH + NO_2 \rightarrow HNO_3 \quad \text{(R17)}$$

Note that Reactions (R14) and (R15) are composite reactions in which the initially formed CH_3CO_2 and CH_3O either decompose and/or react with O_2 to give the products listed.

Reaction (R13) results in underestimation of RO_2NO_2 mixing ratios, whereas Reaction (R14) and subsequent Reactions (R15) and (R16) of organic radical fragments result in an overestimation by oxidising a fraction of any ambient NO. These reactions compete with loss of the organic radical to the wall of the hot quartz tubing or their thermal decomposition so that the size of the artefact will depend non-linearly on ambient levels of NO and NO_2 as well as the concentration of RO_2NO_2. The reaction scheme above indicates that when wall losses of the radicals are neglected, the presence of sufficient NO can result in the generation of three extra NO_2 for each one formed directly in PAN decomposition.

Such effects can be reduced by operating the instrument at very low pressures (and absolute trace gas concentrations) as described by the Berkeley group (Wooldridge et al., 2010). As discussed by Paul et al. (2009), this option is not available for a CRDS instrument which generally operates at higher pressures in order to maintain sufficient sensitivity.

Initial observations of an unchanging mixing ratio when flowing samples of PAN or 2-propyl nitrate at levels of 1–2 ppb through the inlet and cavities at flow rates of between 1 and 3 L (STP) min^{-1} (SLM), and thus varying the reaction time by a factor of 3 indicated that such effects are small, in accord with the observations of Paul et al. (2009) and the data shown in Fig. S3. A detailed experimental investigation of this artefact was conducted in a set of experiments in which known amounts of NO or NO_2 were added to a PAN sample (between 500 and 5000 pptv) and the resultant NO_2 formed by thermal decomposition was monitored.

The results of experiments in which various concentrations of NO_2 were added to three different concentrations of PAN are displayed in Fig. 7. In these experiments, PAN was supplied from a diffusion source of PAN in tridecane held at 273 K.

In the absence of a recombination of $CH_3C(O)O_2$ radicals and NO_2, the difference between $[NO_2]_{TD\ 473}$ and $[NO_2]_{ref}$ (y axis) would be a flat line at the initial PAN

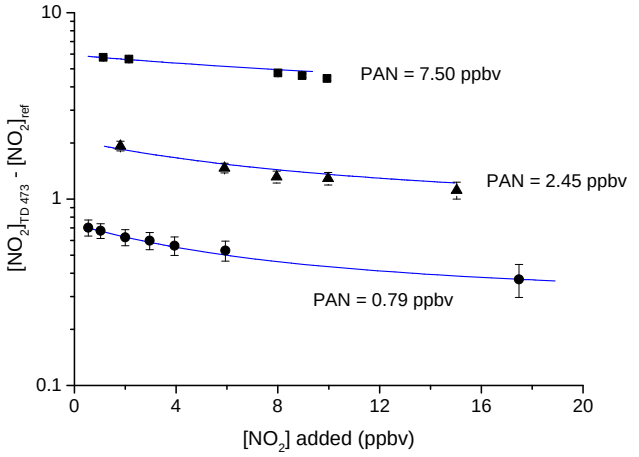

Figure 7. Measurements of the difference signal (TD cavity sampling from the 473 K inlet – NO_2 reference cavity) with various amounts of NO_2 added and at three different PAN concentrations (0.79, 2.45 and 7.50 ppbv). The error bars represent standard deviation and were derived by propagating errors in the NO_2 signals in the TD and reference cavities. The blue lines show the results of numerical simulations as described in Sect. 2.1.7.

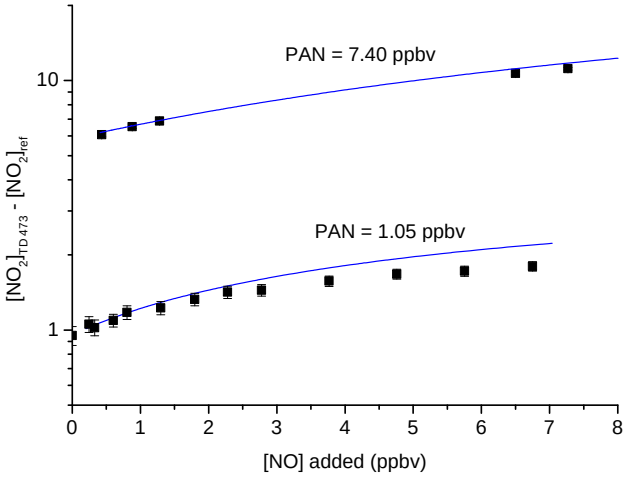

Figure 8. Measurements of the difference signal (TD cavity sampling from the 473 K inlet – NO_2 reference cavity) with various amounts of NO added and at two different PAN concentrations (0.74 and 7.40 ppbv). The error bars represent standard deviation and were derived by propagating errors in the NO_2 signals in the TD and reference cavities. The blue lines show the numerical simulations as described in Sect. 2.1.7. The apparent worsening of the agreement between the model and the experiment at [NO] > 2.5 ppbv is the result of drifts in the PAN mixing ratio during this experiment. By normalising to the PAN concentration (as in Fig. 10), the deviation disappears.

concentration. The effect of reformation of PAN is clearly seen in the data; therefore, at an initial concentration of about 700 pptv of PAN, only 460 pptv would be detected as $[NO_2]_{473} - [NO_2]_{ref}$ if 8 ppb NO_2 were also present. Even in the absence of added NO_2, $[NO_2]_{TD\ 473} - [NO_2]_{ref}$ is smaller than the amount of PAN added as some of the 700 pptv of the NO_2 formed in the thermal dissociation region can also recombine with $CH_3C(O)O_2$.

In Fig. 8 we display the results of a similar set of experiments in which NO was added instead of NO_2. As expected from the reaction scheme above, by adding NO we convert $CH_3C(O)O_2$ radicals into NO_2 and thus observe a positive bias in the $[NO_2]_{TD\ 473}$–$[NO_2]_{ref}$ signal. For an initial PAN concentration of about 1000 pptv, the result of adding 4 pbbv of NO is to overestimate the PAN concentration by about 180 %. These results are similar to those presented in Paul and Osthoff (2010) who used a warmer TD temperature of 523 K (at 450 Torr) and found a roughly linear (negative) dependence on NO_2. They used a second-order polynomial expression to correct the non-linear, positive bias caused by the presence of NO. However, as ambient air contains NO and NO_2 in greatly varying amounts and ratios, there is no simple analytical expression that can provide a correction for the opposing effects of PN underestimation due to NO_2 recombination or PN overestimation as a result of peroxy-radical-induced oxidation of ambient NO. The sign and size of the bias depends on the concentrations of PN, NO and NO_2 and also the rate of wall loss of the peroxy radicals involved (Wooldridge et al., 2010). In order to gain insight into the reactions taking place in the ovens and in the piping leading to the cavities and in the cavities themselves, we conducted a detailed set of numerical simulations (FACSIMILE, Curtis and Sweetenham, 1987) of the laboratory experiments described above.

The simulations were initialised with position-dependent temperature gradients in the oven and subsequent piping and cavities (see Fig. S4), which were derived by inserting a thermocouple into the quartz tubing and measuring the temperature of the inner wall at different distances from the cold, front edge of the oven. As the 473 K oven and cavities were maintained at 800 mbar, the large variation in temperature resulted in significant gradients in the gas density and flow velocity in hot and cold parts of the apparatus, which were also accounted for in the simulations. The gas-phase reactions accounted for in the chemical scheme are listed as supplementary information, the temperature-dependent rate constants being taken mainly from IUPAC (2015). The goal of the simulations was to mimic the observed dependence of the PN–NO_2 signals on the amounts of NO and NO_2 added (i.e. the data in Figs. 7 and 8).

Initial simulations confirmed that the bias due to adding NO and NO_2 was dependent on the assumed wall loss rate constant (k_{wall}) of the HO and peroxy radicals. Simulations with unrealistically large wall loss rates such as to make all other radical reactions insignificant removed the bias completely and thus could not reproduce the observations. The use of very small (or zero) values of k_{wall} resulted in an overestimation of the bias. Although k_{wall} clearly plays a role in

determining the size of the bias, the use of a single value of k_{wall} was not able to reproduce the observed effect for different initial PAN concentrations, with lower values of k_{wall} required for experiments in which PAN was large. This observation is consistent with the radicals being lost to the surface via a Langmuir–Hinshelwood-type mechanism, in which the rates of surface reactions are inversely dependent on radical densities, often described in terms of surface passivation.

The uptake coefficient (γ) for a gas to a surface can be described by the following expression (Crowley et al., 2010a):

$$\frac{1}{\gamma} = \frac{1}{\alpha} + \frac{1}{\Gamma_s} + \frac{1}{\Gamma_d}. \quad (3)$$

Here, α is the accommodation coefficient, which in this case we assume not to be rate-limiting and set as 1. Γ_d is related to diffusive limitation to the uptake and, in tubular geometry, is approximated by

$$\Gamma_d = \frac{3.66(2D_g)}{\bar{c}r}, \quad (4)$$

where r (cm) is the radius of the tube, $\bar{c}$ (cm s^{-1}) is the mean thermal velocity and D_g a diffusion coefficient (cm^2 s^{-1}). Temperature- and pressure-dependent diffusion coefficients for HO, HO_2, CH_3O_2 and $CH_3C(O)O_2$ were calculated from

$$D(R, \text{air}) = \frac{1.0868T^{1.75}}{\sqrt{M(R, \text{air})}\left(\sqrt[3]{V_R} + \sqrt[3]{V_{\text{air}}}\right)^2}, \quad (5)$$

where M is the reduced mass of R in air, R is one of HO, HO_2, CH_3O_2 or $CH_3C(O)O_2$ and V is the diffusion volume, which can be calculated from diffusion volumes for the individual atoms of each radical (Fuller et al., 1966).

In the case of a Langmuir–Hinshelwood reaction, we have

$$\Gamma_s = A\frac{K_{\text{LangC}}}{(1 + K_{\text{LangC}}[R])}. \quad (6)$$

A is a composite term:

$$A = \frac{4k_s[Y]N_{\max}}{\bar{c}}, \quad (7)$$

where k_s is the rate constant for the accommodated trace gas reacting with a surface site Y, and K_{LangC} and $N_{\max}$ describe the equilibrium partitioning of RO_2 to the surface.

We treat A as a variable for optimising agreement between observations and the numerical simulation. In doing this we make some broad simplifications: we take into account the temperature and molecular mass dependence of the mean thermal velocity of HO_2, CH_3O_2 and $CH_3C(O)O_2$ but do not consider the unknown temperature dependence of terms such as k_s and K_{LangC}. We further assume that these terms have the same value for all the peroxy radicals involved and sum the concentrations of the peroxy radicals at each time step, so that $[RO_2]$ in expression (Eq. 8) is equal to $[CH_3C(O)O_2] + [CH_3O_2] + [HO_2]$.

We derive temperature and pressure and thus time-dependent values of γ for each peroxy radical involved. This is then converted to individual wall losses using

$$k_{\text{wall}}(RO_2) = \frac{\gamma\bar{c}}{2r}. \quad (8)$$

The time-dependent values of k_{wall} varied between 0.3 and 0.8 s^{-1} with an average value (over the transport time through the ovens and cavities) of ~ 0.5 s^{-1}, which is similar to the values of 0.2 and 0.3 s^{-1} derived for Teflon and quartz surface reported previously (Wooldridge et al., 2010).

The results of the simulations are shown by the solid blue lines in Figs. 7 and 8. In all cases the same reaction scheme has been applied with only the initial concentration of PAN varied to reproduce the data set. The simulations reproduce the experimental data reasonably well over large variation in PAN ($\sim$ 700 to $\sim$ 7000 pptv) and NO/NO_2, indicating that the reaction scheme is a reasonable representation of the processes taking place. Some deviation (at [NO] > $\sim$ 3 ppb) between the measurement and model for the experiment with PAN = 1.05 ppbv is observed which (at 7 ppbv) amounts to $\sim$ 25 %. This was largely due to fluctuations in the PAN source during this particular experiment and the apparent discrepancy disappears when normalised to the PAN amount, as shown below for the same data set.

The results of one experiment in which both PAN ($\sim$ 560 pptv) and NO (500 pptv) were initially present, and in which NO_2 was varied, are also captured well by the simulations, showing that multicomponent mixtures are also correctly represented (Fig. S6).

One further test was conducted using a photochemical source of PAN which converts NO to NO_2 and then to PAN at a yield of > 90 % (see above). This source is free of NO and NO_2 in significant amounts and can deliver a calibrated PAN amount if the NO mixing ratio is well characterised. The lack of NO_2 in this source was confirmed by observation of (no) NO_2 in the unheated, reference cavity. The cavity sampling from the 473 K oven displayed the expected increase in NO_2, whereas the cold channel showed negligible amounts. The results are displayed in Fig. S7 in which we plot $[NO_2]_{\text{TD 473}} - [NO_2]_{\text{ref}}$ (solid squares) against that calculated from the conversion factor of NO to PAN and the degree of dilution (solid line). The results indicate that the amount of PAN detected is slightly less than calculated at the lowest mixing ratio and that the bias is enhanced at high PAN mixing ratios, consistent with the recombination of $CH_3C(O)O_2$ with NO_2 competing with wall loss of $CH_3C(O)O_2$. The open circles represent the results of a set of simulations (random amounts of PAN) using the same model as described above and initialised with NO and NO_2 mixing ratios of zero. The model reproduces the negligible effect of radical recombination at the lowest PAN mixing ratios and captures the dependence of the bias on PAN over a large range (factor of 10) of PAN mixing ratios, further validating its applicability to systems with varying amounts of PAN, NO and NO_2.

In summary, the model simulations yield correction factors for the amount of NO_2 formed by PAN decomposition, which depends on the mixing ratios of PAN, NO and NO_2. For example, ambient mixing ratios of ∼ 550 pptv PAN, ∼ 520 pptv NO and 2100 pptv NO_2 would result in detection of 518 pptv NO_2 in the TD channel, which thus has a bias of – 32 pptv, requiring a correction factor of 1.06 (i.e. 6 %). For similar PAN and NO_2 concentrations, but with NO reduced to close to zero (e.g. at night) the correction factor increases to 1.28. Correction factors less than unity are only found when NO is in excess of NO_2; e.g. for 550 pptv of PAN with 5100 pptv NO and 1600 pptv NO_2, the correction factor is 0.55.

In Sect. 4 we apply PAN, NO and NO_2 concentration-dependent correction factors to a set of data from a field campaign (PARADE, 2011). In order to do this, the results of > 90 000 simulations were stored in a look-up table from which correction factors for triads of PAN–NO–NO_2 mixing ratios could be read. The results of the full set of simulations are summarised in Fig. S8. As expected, correction factors greater than unity are associated with high NO_2 mixing ratios and those less than unity with large NO mixing ratios. In both cases, the correction factor is smallest when PAN is low (at the limit of zero PAN, there are no RO_2 to recombine with or generate NO_2).

723 K inlet

At the higher temperatures of the 723 K inlet, the chemistry of acetyl and acetyl peroxy radicals is significantly modified compared to that detailed above. The main difference is that the $CH_3C(O)O_2$ radical initially formed in PAN decomposition is thermally instable and can decompose to the acetyl radical (CH_3CO) and O_2 (Reaction R18a) or isomerise to $CH_2C(O)OOH$ (Reaction R18b) (Lee et al., 2002; Carr et al., 2011):

$$CH_3C(O)O_2 + M \rightarrow CH_3CO + O_2 + M \quad \text{(R18a)}$$
$$\rightarrow CH_2C(O)OOH. \quad \text{(R18b)}$$

The major fate of $CH_2C(O)OOH$ is thermal decomposition to OH and a singlet α-lactone (Carr et al., 2011).

$$CH_2C(O)OOH \rightarrow OH + {}^1C_2H_2O_2 \quad \text{(R19)}$$

The acetyl radical formed in (Reaction R18a) can decompose to $CH_3 + CO$ (Reaction R20) or react with O_2 to reform the peroxy radical (Reaction R21a) or form OH (Reaction R21b) and the singlet α-lactone (Tyndall et al., 1995; Carr et al., 2007, 2011; Chen and Lee, 2010; Groß et al., 2014; Papadimitriou et al., 2015):

$$CH_3CO \rightarrow CH_3 + CO \quad \text{(R20)}$$
$$CH_3CO + O_2 + M \rightarrow CH_3C(O)O_2 + M \quad \text{(R21a)}$$
$$CH_3CO + O_2 \rightarrow OH + {}^1C_2H_2O_2 \quad \text{(R21b)}$$
$$CH_3 + O_2 + M \rightarrow CH_3O_2 + M. \quad \text{(R22)}$$

CH_3 formed in Reaction (R20) will react with O_2 to form the methyl peroxy radical (Reaction R22).

At 723 K, Reactions (18)–(21) proceed on timescales of milliseconds or shorter, the net effect being the destruction of $CH_3C(O)O_2$ on a timescale that is short relative to its other loss processes including loss at the wall, recombination with NO_2 or reaction with NO. The radical products formed in these steps are OH and CH_3O_2. The loss of $CH_3C(O)O_2$ at 723 K will obviously reduce the potential for reformation of PAN via Reaction (R13) so that the effect of adding NO_2 should be significantly reduced when compared to the inlet at 473 K. The reaction of CH_3O_2 with NO_2 also forms a peroxy nitrate ($CH_3O_2NO_2$), but one which is unstable with respect to decomposition back to reactants even at moderate temperatures and this reaction does not lead to significant sequestering of NO_2.

The effect of adding NO_2 was explored in a set of experiments with different initial PAN mixing ratios and with NO_2 varied up to ∼ 20 ppbv. The results are displayed in Fig. 9 which plots the ratio of NO_2 from PAN thermal dissociation to the amount of PAN added vs. [NO_2] added. Ideally, in the case of complete dissociation of PAN to NO_2 and no subsequent recombination, this should be close to a value of unity and independent of the mixing ratio of NO_2 added and this is indeed what is observed when sampling from the 723 K inlet. We conclude that at 723 K, there are insufficient peroxy radicals to remove NO_2, and that measurements using this inlet are insensitive to variations in ambient NO_2 up to about 20 ppbv. By way of comparison we also plot the data obtained using the 473 K inlet in the same manner to emphasise the significant dependence on added NO_2 in the cooler inlet as described above. This is consistent with the measurements of Paul et al. (2009) who also observed a lack of dependence on added NO_2 using a 723 K oven operated at a similar pressure (450 Torr).

A similar set of experiments was carried out with NO added instead of NO_2, in this case to investigate potential bias from the oxidation of ambient NO to NO_2 as seen for the 473 K inlet. The results are presented in Fig. 10, which plots the ratio of NO_2 from PAN thermal dissociation to the amount of PAN added vs. [NO] added. In the absence of any unwanted NO_2 formation resulting from NO oxidation, the result should be a flat line with an intercept of 1. Figure 10 shows that NO is converted to NO_2 in the 723 K inlet, though the effect is much reduced when compared to the 473 K inlet. For example, the effect of adding 10 ppb NO is to bias the PAN measured by a factor 2.75 sampling from the 473 K inlet and 1.5 when sampling from the 723 K inlet. There is no significant difference in the bias when PAN was varied between 1 and 2.5 ppb. Note that the data plotted here for the 473 K inlet are the same as those in Fig. 8.

As described in detail above, the large bias seen when sampling from the 473 K inlet results mainly from reactions of $CH_3C(O)O_2$ with NO. As $CH_3C(O)O_2$ decomposes rapidly at 723 K, the oxidation of NO to NO_2 at this temperature

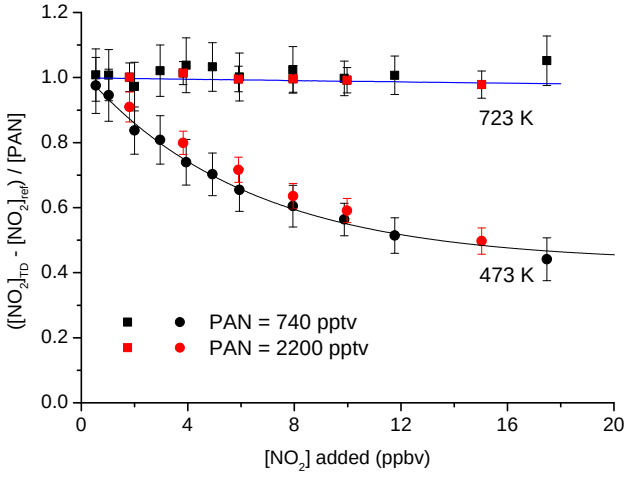

Figure 9. Measurements of the difference signal (TD cavity sampling from the 473 (squares) or 723 K inlet (circles) – NO_2 reference cavity) when adding different amounts of NO_2 to PAN samples (740 or 2200 pptv). $[NO_2]_{TD}$ refers to the mixing ratio of NO_2 measured in the TD cavity sampling from either the 473 or 723 K inlet. The blue line denotes the model prediction of the effect of adding NO_2 to the 723 K inlet. The black line shows an exponential fit to the NO_2 measured when sampling from the 473 K inlet and is added to guide the eye. The error bars represent standard deviation and were derived by propagating errors in the NO_2 signals in the TD and reference cavities.

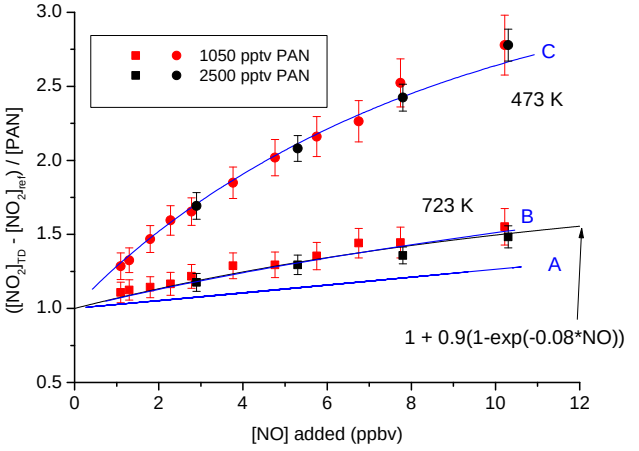

Figure 10. Measurements of the difference signal (TD cavity sampling from the 473 (squares) or 723 K inlet (circles) – NO_2 reference cavity) when adding various amounts of NO to PAN samples (1000 or 2500 pptv). $[NO_2]_{TD}$ refers to the mixing ratio of NO_2 measured in the TD cavity sampling from either the 473 or 723 K inlet. The simulations (blue lines) labelled A and B are model predictions of the effect of adding NO_2 to the 723 K inlets using different rate constants for the rearrangement of $CH_3C(O)O_2$ to $CH_2C(O)OH$ (see text for details). The simulation labelled C corresponds to the 473 K inlet. The error bars represent standard deviation and were derived by propagating errors in the NO_2 signals in the TD and reference cavities. The black lines show exponential fits to the data as described by the expressions given.

is expected to be via the CH_3O_2 radicals formed in Reactions (R20)–(R22) and also via conversion of CH_3O_2 to HO_2 in the presence of NO/O_2 (Reaction R15). This could be qualitatively confirmed by extending the simulations described above to cover the temperatures of the 723 K inlet. In order to do this, we scaled the temperature profile to peak at 723 K (instead of 473 K) and also added Reactions (R18)–(R22). The rate coefficients used were from Baulch et al. (2005) (Reaction R20), (Papadimitriou et al., 2015) (Reaction R21a and R21b) with the dissociation and isomerisation rate constants taken from Lee et al. (2002). We note that, as these rate constants are poorly characterised at 723 K and that, even at 298 K, there is disagreement concerning e.g. the yield of OH from $CH_3CO + O_2$ (Carr et al., 2007; Groß et al., 2014; Papadimitriou et al., 2015), perfect agreement between observation and simulation is not expected. The simulation shown in Fig. 10 (blue line, labelled A) does however capture the observed reduction in oxidation of NO to NO_2 in the 723 K inlet compared to the 473 K inlet (blue line, labelled "C"). Simulation C was obtained using the same simulation but with the temperature profile for the 473 K inlet.

The amount of NO_2 formed depends on the abundance of CH_3O_2 and HO_2, so that the simulated NO_2 generation is favoured by higher rates of $CH_3C(O)O_2$ dissociation to CH_3CO rather than isomerisation to $CH_2C(O)OOH$, and higher rates of CH_3CO dissociation to CH_3 relative to reaction with O_2, which ultimately leads to OH (which can remove NO_2 by forming HNO_3) rather than CH_3O_2 or HO_2. An improved match between the observation and the model (Fig. 10, blue curve marked "B") was achieved by reducing the rate of isomerisation of $CH_3C(O)O_2$ to $CH_2C(O)OOH$ to 20 % of the value reported by Lee et al. (2002) at 723 K. This value is strongly dependent on calculated barrier heights and is particularly uncertain, as has been noted by Carr et al. (2011). We do not seek to imply that our data constrain such kinetic parameters as there are certainly other factors that can affect the NO_2 production rate, including the rates of wall losses of radicals and the relative rates of decomposition and isomerisation of $CH_3C(O)O_2$ and the thermal stability of CH_3CO.

In summary, in the absence of ANs, the experiments sampling PAN via the 723 K inlet reveal that there is no significant bias when adding NO_2, and that the (positive) bias introduced by the addition of NO is independent of the amount of PAN, at least up to 2–3 ppbv PAN. This simplification of the chemistry compared to the 473 K inlet removes the need for complex simulations to correct the data set. The NO_2 mixing ratio resulting from the presence of PAN and NO in the 723 K inlet is adequately described by the expression $PAN^* (1 + 0.9(1 - \exp(-0.08^*NO)))$, with NO being the NO mixing ratio in ppb (solid black line in Fig. 10), which returns correction factors of 0.94 at 1 ppb NO and ∼ 0.64 at

$\sim$ 10 ppbv NO and is valid for NO mixing ratios up to about 10 ppbv. These NO-dependent factors must be applied to the PAN mixing ratios prior to subtracting them from the total NO_2 signal (from ΣANs + ΣPANs) when sampling from the 723 K inlet.

We now consider the chemistry taking place when ANs are present. For the 723 K inlet and considering 2-propyl nitrate, the additional reactions are

$$2\text{-}C_3H_7ONO_2 \rightarrow 2\text{-}C_3H_7O + NO_2 \quad \text{(R23)}$$

$$2\text{-}C_3H_7O + O_2 \rightarrow CH_3C(O)CH_3 + HO_2 \quad \text{(R24)}$$

$$2\text{-}C_3H_7O + M \rightarrow CH_3 + CH_3CHO + M \quad \text{(R25)}$$

$$HO_2 + NO \rightarrow NO_2 + OH. \quad \text{(R26)}$$

The CH_3 radical is immediately converted to CH_3O_2 so that the radical pool is again a mixture of CH_3O_2 and HO_2, both of which may convert NO to NO_2. As neither $CH_3O_2NO_2$ nor HO_2NO_2 are sufficiently thermally stable to sequester NO_2 these radicals should not lead to loss of NO_2 via recombination. In the 723 K inlet, this chemical system should therefore behave similarly to the one described above for PAN, i.e. should suffer from positive bias when adding NO but no negative bias when adding NO_2.

The results from a set of experiments to explore the effects of adding NO_2 to various amounts of 2-propyl nitrate are displayed in Fig. 11. NO_2 was varied between $\sim$ 0.5 and 12 ppb for 2-propyl nitrate mixing ratios of 0.35, 0.75 and 2.6 ppb. The bias from adding NO_2 at these levels is not measurable at the lowest 2-propyl nitrate mixing ratios, though the data at 2.6 ppb indicate a weak reduction in the measured AN mixing ratio. The model described above was extended with Reactions (R23) to (R26) and initiated with the 2-propyl nitrate mixing ratios observed in the absence of extra NO_2. The results are shown by the blue lines in Fig. 11. Once again the model satisfactorily predicts the trends observed for each experiment, including the weak loss (5 %) of NO_2 observed at the highest 2-propyl nitrate mixing ratio. The simulations revealed that the sole significant "reservoir" of this missing 5 % of 2-propyl nitrate was in the form of $CH_3O_2NO_2$.

Experiments with various amounts of added NO are summarised in Fig. 12. The positive bias caused by oxidation of NO to NO_2 is apparent, and at NO mixing ratios of 8 ppb, results in a $\sim$ 60 % overestimation of the 2-propyl nitrate mixing ratio. The model (blue lines) also indicates that this is expected, the main oxidant of NO being CH_3O_2. The effect of adding 5 ppb of NO_2 is not observable, consistent with the weak effects described above in the absence of NO_2.

A more detailed look at the relative bias caused by adding NO is provided by Fig. 13, which plots the ratio of the AN signal in the presence of NO to that without added NO. There is no clear trend in the data set with the largest effects (i.e. the uppermost and lowermost data points not associated with the extremes of 2-propyl nitrate mixing ratios. The positive bias caused by the presence of NO is adequately described by the expression $1 + 1.8(1 - \exp(-0.08^{*}\text{NO}))$, with NO being

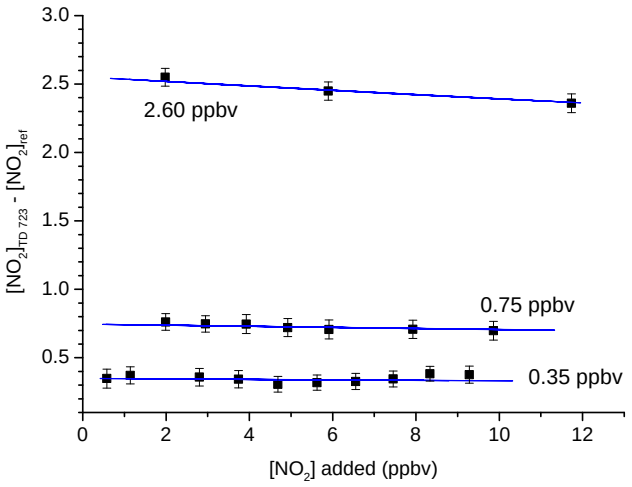

Figure 11. Measurements of the difference signal (TD cavity sampling from the 723 K inlet – NO_2 reference cavity) when adding different amounts of NO_2 to 2-propyl nitrate samples (0.35, 0.75 or 2.6 ppbv). The error bars represent standard deviation and were derived by propagating errors in the NO_2 signals in the TD and reference cavities. The blue lines show the model predictions of the effect of adding NO_2 to the 723 K inlet as described in the text.

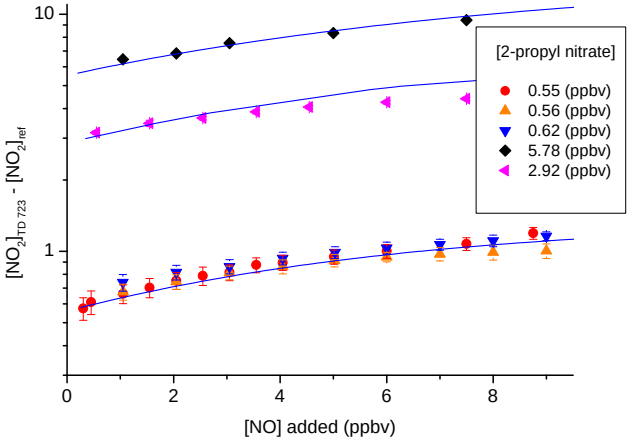

Figure 12. Measurements of the difference signal (TD cavity sampling from the 723 K inlet – NO_2 reference cavity) when adding different amounts of NO_2 to 2-propyl nitrate samples (0.55, 0.56, 0.62, 2.92 or 5.78 ppbv). The sample with 0.62 ppbv 2-propylnitrate also contained $\sim$ 5 ppbv of NO_2. The error bars represent standard deviation and were derived by propagating errors in the NO_2 signals in the TD and reference cavities. The blue lines show the model predictions of the effect of adding NO to the 723 K inlet as described in the text.

the NO mixing ratio in ppb. This is plotted as the solid black line in Fig. 13. The blue lines indicate the model prediction when initialised with 0.56 (upper blue line) and 5.78 ppbv (lower blue line) 2-propyl nitrate, respectively. The model correctly predicts the strong response of adding NO and the

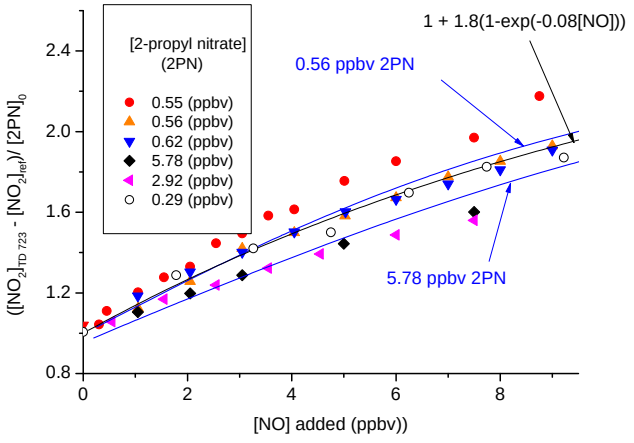

Figure 13. Relative change in difference signal $([NO_2]_{TD\,723} - [NO_2]_{ref}) / [2PN]_0)$ as a function of added NO for six different 2-propyl nitrate (2PN) mixing ratios. $[2PN]_0$ is the measured mixing ratio of 2-propyl nitrate in the absence of added NO. The sample with 0.62 ppbv 2-propyl nitrate also contained ~ 5 ppbv of NO_2. The black line is defined by the expression $([NO_2]_{TD\,723} - [NO_2]_{ref}) / [2PN]_0) = 1 + 1.8 \times (1 - \exp(-0.08[NO]))$, where [NO] is the mixing ratio of NO in ppbv. The blue lines show model results with 0.56 and 5.7 ppbv 2-propyl nitrate.

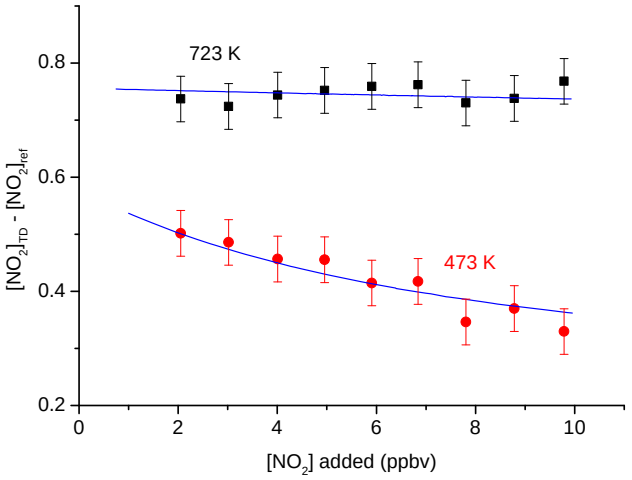

Figure 14. Dependence of $([NO_2]_{TD\ 473} - [NO_2]_{ref})$ and $([NO_2]_{TD\,723} - [NO_2]_{ref})$ on added NO_2 in the presence of PAN (0.53 ppbv) and AN (0.19 ppbv). The error bars represent standard deviation and were derived by propagating errors in the NO_2 signals in the TD and reference cavities. The blue lines show the model results as described in the text.

weak effects caused by using two different 2-propyl nitrate concentrations that differ by a factor of ~ 10.

We conclude that the (negative) bias caused by addition of NO_2 to samples of 2-propyl nitrate is small and, to a good approximation, independent of the 2-propyl nitrate mixing ratio. The positive bias caused by oxidation of NO (by CH_3O_2) is sufficiently large to require correction, the appropriate factor given by the inverse of the expression $1 + 1.8(1 - \exp(-0.08^*\mathrm{NO}))$.

As a final test of our understanding of the chemistry, experiments were conducted in which the four components, NO (0.5 ppbv), NO_2 (varied), PAN (0.53 ppb) and 2-propyl nitrate (0.19 ppb), were present. The results are displayed in Fig. 14. The model (blue lines) correctly predicts the total signal observed in both channels, allowing us to conclude that within experimental error, the model chemistry simulates the effects of radical recombination and radical-induced oxidation of NO to NO_2 in both inlets/cavities.

In summary, the correction procedure when sampling from the 453 and 723 K inlets is as follows. (1) We use the model simulation results in the form of look-up tables with measured NO and NO_2 concentrations and the total signal $[NO_2]_{TD\ 473} - [NO_2]_{ref}$ to derive (by inversion) the correct PAN mixing ratios. (2) This PAN mixing ratio is used to calculate its (NO-dependent) contribution to the observed total NO_2 measured when sampling from the 723 K inlet. This contribution is subtracted and the result divided by $1 + 1.8(1 - \exp(-0.08^*\mathrm{NO}))$. This leads to the final expression to derive corrected ΣANs:

$$[\mathrm{ANs}] = \frac{[NO_2]_{TD\ 723} - [NO_2]_{ref} - [\mathrm{PAN}]\,F1}{F2}, \quad (9)$$

with correction factors $F1 = 1 + 0.9(1 - \exp(-0.08[\mathrm{NO}]))$ and $F_2 = 1 + 1.8(1 - \exp(-0.08[\mathrm{NO}]))$, where [i] are mixing ratios in ppbv. When the NO mixing ratio is zero, Eq. (9) reduces to $[\mathrm{ANs}] = [NO_2]_{TD\,723} - [NO_2]_{ref} - [\mathrm{PAN}]$.

The laboratory tests we describe above provide insight into the radical reactions that take place in the heated inlets. The tests were conducted with PAN as a representative peroxy nitrate and with 2-propyl nitrate representing alkyl nitrates. Although the initial thermal decomposition of other PNs and ANs is likely to be follow a very similar pattern (Day et al., 2002; Wooldridge et al., 2010; Perring et al., 2013), we cannot rule out that the organic radicals, formed with, e.g. different functional groups, will behave somewhat differently and would thus require modified correction factors. Comparison with instruments measuring both speciated and summed PNs and ANs would be required to examine this.

2.1.8 Other absorbing trace gases at 405–408.5 nm

The potential for systematic error owing to light absorption at 405 or 408.5 nm is limited to a small number of trace gases that absorb at such wavelengths. Those known to be present in the atmosphere are dicarbonyls, such as glyoxal (CH(O)CH(O)), methylglyoxal ($CH_3C(O)CH(O)$) and biacetyl ($CH_3C(O)CH_3C(O)$), which are formed from the degradation of many volatile organic compounds including isoprene and aromatics (Atkinson, 1994; Calvert et al., 2000, 2002). The absorption cross sections of these dicarbonyls at

wavelengths between 405 and 410 nm are approximately 6 $(\pm 2) \times 10^{-20}$ cm^2 molecule^{-1} (Meller et al., 1991; Atkinson et al., 2006; IUPAC, 2015), about a factor 10 lower than those of NO_2 (see Fig. 2). Although high mixing ratios of e.g. glyoxal (> 1 ppbv) have been observed in polluted environments (Volkamer et al., 2005a), its contribution to absorption is estimated to be insignificant compared to NO_2 (Fuchs et al., 2009). In rural environments, peak mixing ratios of glyoxal and methylglyoxal of up to 200–300 pptv have been reported (Lee et al., 1995; Huisman et al., 2011). This would generate a bias of ∼ 20–30 pptv in the NO_2 measurement, which corresponds to an error of 5 % if NO_2 levels are less than ∼ 400 pptv.

NO_3 radicals also absorb at 405 nm, with a cross section of $\sim 3 \times 10^{-20}$ cm^2 molecule^{-1}, i.e. a factor of 20 less than NO_2. NO_3 mixing ratios of several hundred pptv (only at night) have been reported (see e.g. Crowley et al., 2010b) so that the NO_3 contribution to extinction at ∼ 400 nm could exceed that of the dicarbonyls discussed above. However, as NO_2 serves as precursor to NO_3, its mixing ratios are always much larger; therefore, even if NO_3 were efficiently sampled into the cavity, its contribution to absorption at 405 nm would be negligible.

2.1.9 Detection of N_2O_5 (473 K) and $ClNO_2$ (723 K)

Numerous studies have reported the measurement of N_2O_5 via thermal dissociation at temperatures between 80 and 100 °C to NO_3, which may be detected by CRDS at 662 nm (see e.g. Brown and Stutz, 2012, and references therein). As the co-product of the thermal dissociation is NO_2, the presence of N_2O_5 also represents a potential interference when sampling from either of the heated inlet lines. We have used the thermal dissociation of N_2O_5 and detection of NO_2 using CRDS at 405 nm to detect N_2O_5 in this manner in laboratory investigations (Tang et al., 2012).

N_2O_5 is not present in significant mixing ratios during the day but can represent a significant fraction of oxidised nitrogen at night-time. In the data set obtained in the PARADE campaign, we observed occasional increases in NO_2 when sampling from the heated inlets that were strongly correlated with the presence of N_2O_5 (measured by TD-CRDS at 662 nm, Crowley et al., 2010b). Correction for an N_2O_5 contribution could however not be accurately applied as the sampling efficiency (through ≈ 10 m of PFA tubing) was unknown but evidently less than unity as the features observed in the NO_2 instrument were weaker than those in the N_2O_5 instrument. In addition, the NO_3 formed may also react with any NO available (generating two more NO_2) or with hydrocarbons, so that the stoichiometry of N_2O_5 to NO_2 conversion may be variable.

For the PARADE campaign data set we therefore chose to eliminate data during episodes of high N_2O_5 (> 150 pptv). We conclude that undesired detection of N_2O_5 as NO_2 when sampling from the heated inlets can be a significant source of uncertainty when measuring ΣPN at night-time, especially if measurements of N_2O_5 are not available. As both heated channels will decompose N_2O_5 to NO_2 the measurement of the ΣANs (obtained as the difference signal) should not be impacted by the presence of N_2O_5.

A potential interference specific to the 723 K channel results from the thermal decomposition of $ClNO_2$, which is formed in the heterogeneous reaction of N_2O_5 on chloride-containing particles at night-time. In a series of laboratory experiments using this instrument (Fig. S9) we showed that a sample of $ClNO_2$ was detected as NO_2 at oven temperatures above ∼ 680 K, consistent with that reported by Thaler et al. (2011). As $ClNO_2$ can represent a significant fraction of NO_2 at night-time and in the early morning (see. e.g. Osthoff et al., 2008; Thornton et al., 2010; Phillips et al., 2012; Wagner et al., 2012; Mielke et al., 2013) it will represent a significant source of uncertainty in the measurements of the ΣANs when present. In this case, the only correction possibility requires the simultaneous measurement of $ClNO_2$. During the PARADE campaign (see later), early-morning $ClNO_2$ levels approached 800 pptv; therefore large corrections had to be applied to extract ΣANs during these periods.

2.1.10 Precision

The precision of the measurements of NO_2 in the reference cavity and TD cavities was derived by continuous sampling of zero air. Equivalent NO_2 mixing ratios were calculated for conditions of 893 mbar and 35 °C. The results are summarised in Fig. 15 where the upper panel shows the raw data converted to NO_2 mixing ratio equivalents. The regular spaces in the data are zeroing periods as they would have been measured in a normal experiment. The baseline which is plotted for a 2 h time interval here shows no long-term trend, indicating that the zero measurements every 5–10 min are sufficient to capture drifts in ring-down related to the variability of the cavity performance. The lower panel is an Allan deviation plot for this cavity (red curve), which shows that the 1σ precision improves for integration times up to ∼ 40 s and follows the expected square root dependence (red, dashed line) up to an integration time of ∼ 10 s. The precision at 1 s integration time is 28 pptv, improving to 5–6 pptv at 40 s.

The precision obtained with the TD cavity (sampling from the 723 K inlet) was investigated by adding a constant mixing ratio (∼ 700 pptv) of 2-propyl nitrate and measuring the difference signal between the reference and TD cavities. These results are shown in the middle panel (raw data) and in the Allan deviation plot (blue lines). The precision of the measurement improves from ∼ 10 % for 4 s integration time to about 3 % for 1 min integration time and follows a square root dependence up to ∼ 10 s integration time.

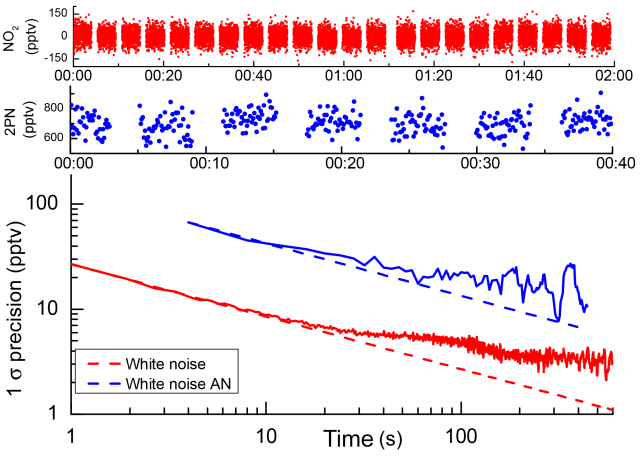

Figure 15. The upper panel (red data points) displays a time series of raw NO_2 data (5 s intervals) when sampling zero air. The middle panel (blue data points) shows a series of measurements when sampling a constant flow of 2-propyl nitrate ($\sim$ 700 pptv) from the 723 K inlet. The lower panel is an Allan deviation plot showing the dependence of the measurement precision ($1\,\sigma$) on the signal integration time in the reference cavity (red curve) and TD cavity (blue curve). The dashed lines represent precision expected for random noise.

2.1.11 Total uncertainty

NO_2 measurement

Several sources of systematic error may contribute to the total uncertainty of the NO_2 measurements in the reference cavity; these are as follows:

- error in determination of the effective cross section σ_{Laser}: ≤ 5 %, which also accounts for uncertainty in the absolute NO_2 cross sections of Voigt et al. (2002);
- wavelength stability of the laser emission over longer measurement periods: ≤ 3 % based on variability of the emission spectra (recorded at 20 min intervals);
- error in l/d ratio: ~ 1 % (see above);
- error in pressure and temperature stability of the cavities: ~ 0.5 %;
- NO_2 mixing ratio in zero air bottles: < 20 pptv (see above);
- error in humidity correction: considering the difference in values of $\Delta\sigma_{Rayleigh}^{405-409\,nm}$ derived in this work and those of Fuchs et al. (2009) (see Sect. 2.1.3) we estimate an error of about 20 % in this correction factor; this converts to an error of ≤ 20 pptv at 100 % RH;
- possible interference from other absorbers: normally negligible but must be assessed on a case-to-case basis.

At very low NO_2 mixing ratios, the uncertainty of the NO_2 measurements is therefore mainly influenced by the amount of NO_2 within the zero air bottles and the correction applied for the scattering effect of ambient H_2O, whilst at larger NO_2 mixing ratios, the uncertainty is mainly determined by the uncertainty in the effective cross section and laser stability. The uncertainty of the NO_2 measurement stemming from systematic errors is thus 6 % + 20 pptv + (20 pptv*RH/100), where RH is in percent. For any given integration period, the total uncertainty may be obtained by adding the precision quoted above and is e.g. 11 % + 30 pptv for a 40 s sampling period, with a relative humidity of 50 %.

Measurement of PNs

As this is a difference measurement, the uncertainty in the corrections for the potential presence of NO_2 in the zero air or errors in $\Delta\sigma_{Rayleigh}^{405-409\,nm}$ do not contribute to overall uncertainty. The major source of uncertainty is associated with the corrections made for reactions of radical fragments with NO and NO_2 (Sect. 2.1.7). Although performing the correction via modelling of the chemistry in the hot inlets and subsequent tubing is clearly complex, the fact that laboratory data covering a large parameter space can be simulated well indicates that the error in the correction is less than 15 % at the largest PAN, NO and NO_2 mixing ratios investigated. However, as we have only performed these tests for PAN and not for other peroxy acyl nitric anhydrides, we increase the maximum uncertainty on this correction factor to a conservative estimate of 30 %. As the size of the correction increases non-linearly with each of PAN NO and NO_2 mixing ratios, no single uncertainty can be given. As an example, at 1 ppb PAN, the correction factor required in the presence of 1 ppb NO and 5 ppb NO_2 is 1.09 ± 0.22. In the absence of NO (e.g. at night-time) the same concentrations of PAN and NO_2 require a correction factor of 1.52 ± 0.30.

Measurement of ANs

As the instrument has only two measurement cavities sampling from three inlets, the derivation of ΣANs while sampling from the 723 K inlet requires interpolation of the measurements from the 473 K inlet. The overall uncertainty for the measurements of the ΣANs thus depends on the variability of the measurements of the ΣPNs. A further source of uncertainty is associated with the corrections made for reactions of radical fragments with NO and NO_2 as described in Sect. 2.1.7. The largest errors in ΣANs will be associated with air masses with high ΣPN and low ΣANs, as this will amplify any error in the correction related to the different efficiency of sampling of ΣANs from both inlets, which itself is a function of the NO and NO_2 concentrations. For example, using expression Eq. (9), and adding a $[NO_x]$-dependent error to the PAN, F1 and F2 correction factors (increasing from 0 to 10 % error when going from

0 to 5 ppb NO), we calculate a total possible error of ∼ 16 % if $[NO_x] = [PAN] = 1$ ppb, increasing to ∼ 50 % at 5 ppb of NO.

Clearly, the accuracy of the ΣPN measurement and its correction will critically impact on the accuracy of the ΣAN measurement. As we indicate later, reliable ΣAN measurements are made under certain conditions (low PAN variability and $[NO_2] < \sim 5$ ppbv).

3 Ambient data sets for NO_2, ΣPNs and ΣANs

A summer field campaign of ∼ 3 weeks' duration at the Taunus Observatorium on the Kleiner Feldberg (Crowley et al., 2010b; Phillips et al., 2012) provided opportunity for comparison of the present CRDS system for measurement of NO_2 and ΣPNs with established instruments under variable conditions. The Taunus Observatorium is in a rural area impacted by emissions from several local sites between 30 and 40 km distance away. Typical NO_x levels are between 1 and 2 ppb, with occasional excursions up to peak values of > 10 ppb (Crowley et al., 2010b). Summertime PAN levels of at the site had been reported as part of a PhD thesis with, campaign averaged, mid-afternoon maximum concentrations of about 1 ppb (Handisides, 2001).

3.1 NO_2 measurements

The established instruments used for comparison were (for NO_2) a chemiluminescence detector (CLD) with a blue-light converter and a long-path differential optical absorption spectrometer, DOAS. These instruments are described in detail elsewhere (Crowley et al., 2010b; Pöhler et al., 2010; Hosaynali Beygi et al., 2011; Merten et al., 2011; Suitters, 2012).

TD-CRDS vs. CLD

Both instruments sampled air via PFA tubing with co-located inlets about 8 m above ground level and 2 m above the platform structure to which the inlets were attached. In both cases, bypass flows were used to reduce the residence time in the inlets. The TD-CRDS sampled at a rate of ∼ 0.2 Hz, the CLD at ∼ 1 Hz. The accuracy of the CLD measurements, defined partially by calibration accuracy, blue-light converter efficiency, and assumptions about levels of NO_2 in zero air, is reported to be ∼ 10 % during the PARADE campaign (Li et al., 2015).

The data displayed in Fig. 16 (upper panel) show the correlation between 1 min averaged NO_2 mixing ratios derived by these two instruments. The error bars are the reported standard deviation over the sampling interval, and reflect atmospheric variability rather than instrument precision. Agreement is good, with a slope 0.906 ± 0.0003 for the bivariate (York) fit to the data and an intercept of -115 ± 0.7 pptv. An unweighted fit gives values of 0.889 ± 0.0006 and

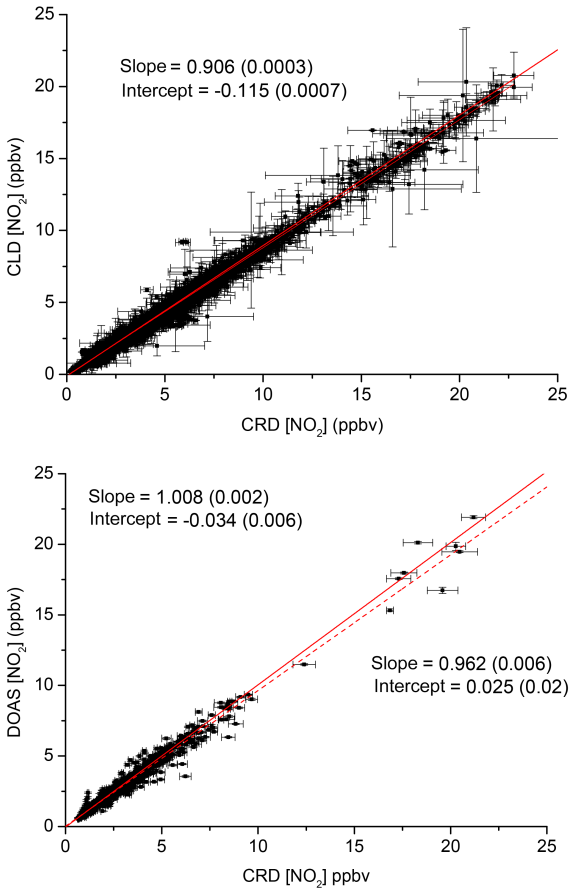

Figure 16. Comparison of NO_2 data (reference cavity) from the TD-CRDS with two established instruments. Upper panel: chemiluminescence detector (CLD), 1 min data averages. Lower panel: long-path differential absorption spectrometer (DOAS), 10 min data averages. The red solid lines are weighted bivariant fits considering reported standard deviations for both instruments; the dashed line is an unweighted fit. For the DOAS comparison, only data were used for which the CRDS indicated standard deviations of less than 5 % (over 10 min intervals).

-86 ± 2 pptv. Irrespective of the method of weighting used, the deviation of the slope from unity lies within the combined uncertainty of the instruments. A statistically significant, negative intercept as observed would be e.g. the result of low levels (∼ 100 pptv) of NO_2 present in the zero air used to zero the CLD, or the photochemical/surface-activated decomposition (to NO_2) of surface adsorbed trace gases (e.g. nitrates) in the blue-light converter during zeroing.

CRDS vs. DOAS

The lower panel of Fig. 16 shows the correlation between the CRDS and DOAS instruments. The DOAS measured NO_2 over an optical path length of ≈ 3 km, with the light source and spectrograph located within a few metres of the CRDS inlet. The DOAS measurements of NO_2 were made

every 10 min. Spatial inhomogeneity in NO_2 mixing ratios will result in reduced agreement between a point measurement (CRDS) and that of the DOAS, which integrates over a large area. For this reason we compare only data in which the temporal variability in the CRDS signal results in standard deviations over the 10 min averaging interval of less than 5 %. Such data sets are likely to be characterised by good spatial homogeneity over the same time period and are more suitable for comparison. The resulting slope and intercept from the weighted, bivariant fit are 1.008 ± 0.002 and -0.034 ± 0.006 ppbv, respectively. The unweighted fit resulted in values of 0.962 ± 0.006 and 0.025 ± 0.002 ppbv, respectively, both fits indicating excellent agreement between these instruments.

We conclude that the CRDS measurements of NO_2 compare well with two well-established instruments, confirming the experimental concept and the accuracy of the correction factors applied.

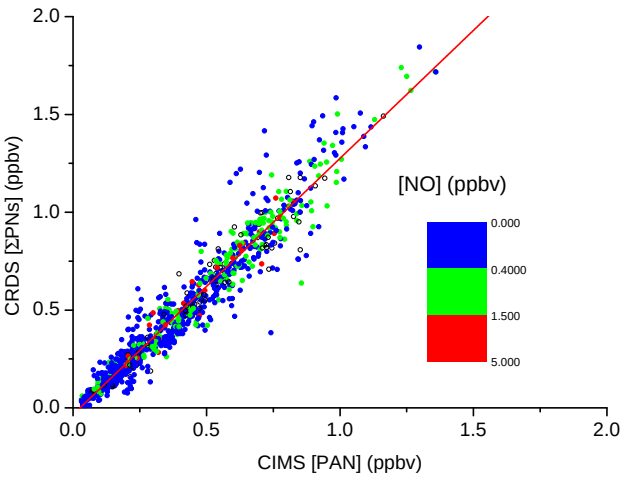

Figure 17. PARADE data: comparison of PAN derived by the TD-CIMS with the TD-CRDS measurement of ΣPNs. The ΣPNs data have been corrected as described in the text. The data are colour-coded according to [NO] mixing ratios.

4 Measurement of ΣPNs and comparison with PAN measured by TD-CIMS

During PARADE, speciated PANs were measured using a TD-CIMS (Phillips et al., 2013). The CIMS instrument is able to distinguish between different acyl peroxy nitrates such as PAN, PPN or MPAN, while the TD-CRDS measures the sum of all the individual nitrates. The TD-CIMS requires an in situ calibration using a photochemical source of PAN. This PAN calibration source was characterised using the TD-CRDS instrument, employing the correction factors described above. As the calibration was conducted at ~ 500 pptv of PAN, and in the absence of extra NO_2 or NO, the correction factor for the CRDS measurements (1.06) was small.

Figure 17 shows the comparison between the PAN measurements by CIMS and ΣPNs measured by the TD-CRDS. The correlation between the measurements is very good ($R^2 = 0.93$), with a slope of 1.31 and an intercept of -34 pptv. The data are coloured according to [NO] and indicate no obvious bias due, e.g., to the existence of high NO levels. The correction factors applied to the TD-CRDS data set were in the range of 0.8–1.5, mostly however close to 1.15 ± 0.1. This is illustrated in the frequency distribution plot in Fig. S10.

The slope of greater than unity indicates the presence of peroxy nitrate species such as PPN, MPAN and APAN, which thus represent ~ 24 % of total PNs. In addition to PAN, the TD-CIMS monitored five masses corresponding to other PNs. These masses have not been calibrated, though by assuming the same detection efficiency as PAN, we can show that PNs other than PAN represented ~ 20 % of all PNs, consistent with the value above. The PAN and measurements of ΣPNs will be discussed in detail in a publication describing the results of the PARADE campaign. Here we simply note that the results are consistent with previous observations, which indicate that PAN is the most abundant PN in the atmosphere and usually contributes 70–90 % of the total peroxy nitrates (Roberts, 1990).

5 Measurements of ANs

A 5 day period of measurements of ΣANs with NO_2, NO and ΣPNs during PARADE is shown in Fig. 18. The black data points in the ΣPNs plot (lower panel) denote the raw data; the red data points have been corrected for the effects of NO and NO_2 as derived above. The black data points in the ΣANs plot (middle panel) indicate the total NO_2 signal when sampling from the 723 K inlet minus the NO_2 measured in the reference cavity, and thus represent the uncorrected sum of ΣANs + ΣPNs. The red data points were obtained by applying the full corrections as described. To illustrate the magnitude of the corrections, this may be compared to the blue data points which were obtained simply by subtracting the NO_2 mixing ratios measured when sampling from the 473 K inlet from that when sampling from the 723 K inlet. The difference between the blue (uncorrected) and red (corrected) data sets is mainly less than ~ 20 % but can be much larger during episodes of high NO and NO_2. For a particular set of conditions, the most reliable data (i.e. small correction factors) were obtained for $NO_x < 5$ ppb. As noted above, a more detailed analysis of this and the ΣPNs data set will be presented elsewhere.

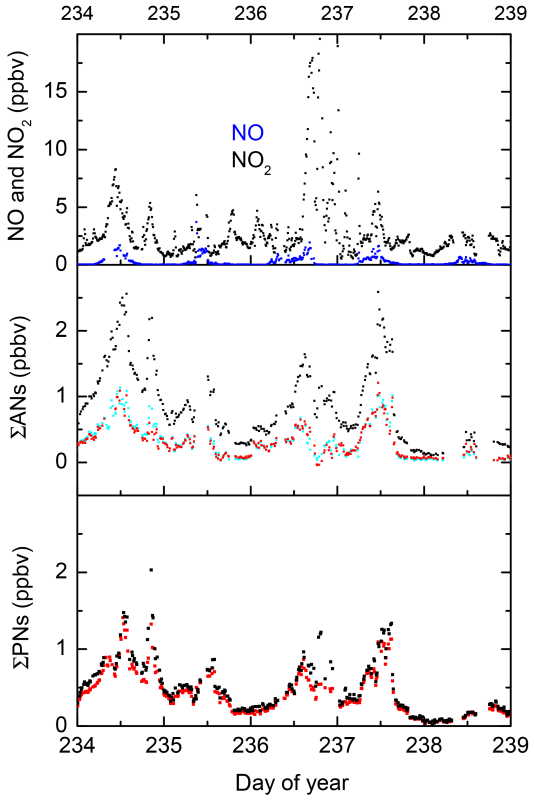

Figure 18. Time series of PARADE data over a 5 day period. Upper panel: NO_2 mixing ratios (black data points) measured in the reference cavity along with NO measured by the CLD (blue data points). Central panel: TD cavity measurements when sampling from the 723 K inlet. Black data points indicate uncorrected (raw) data. The blue data points were obtained by directly subtracting the NO_2 mixing ratios measured when sampling from the 473 K inlet from that when sampling from the 723 K inlet. The red data points include the corrections described in the text. Lower panel: uncorrected (black) and corrected (red) measurements of the ΣPNs.

6 Conclusions and outlook

We have developed, tested and deployed a two-cavity (405.2 and 408.5 nm) instrument with three different inlets for the measurement of ambient NO_2, ΣPN and ΣAN. NO_2 is measured directly with a total uncertainty of $6\% + 20$ pptv + (20 pptv*RH/100), where RH is in percent. PNs and ANs are detected via thermal dissociation to NO_2, and extensive laboratory characterisation of the instrument, including numerical simulation of the radical chemistry in both heated inlets, was carried out in order to derive correction factors that account for the bias caused by the competing effects of radical recombination and oxidation of ambient NO. The requirement to correct the ΣAN and ΣPN data sets limits the application of this prototype instrument to regions of low to moderate NO_x levels (< 5 ppb).

The first field deployment (PARADE) showed favourable comparison with other NO_2 and ΣPN measurements (chemiluminescence detector with blue-light converter and long-path differential optical absorption spectroscopy for NO_2, and chemical ionisation mass spectrometry for ΣPNs). During the campaign, the correction factor for PNs was, on average, between 0.8 and 1.2, depending on the relative NO and NO_2 concentrations.

Future improvements will involve the use of humidified zero air to reduce uncertainty resulting from optical scattering of atmospheric water vapour, which will improve the accuracy of the data at low NO_x levels. We shall also explore other signal acquisition hardware/software options, with the goal of increasing the sampling rate and improving the detection limit for all channels. We will add an extra cavity to enable permanent sampling from all three inlets, removing the need to interpolate data from the 473 K inlet.

Most importantly, we shall investigate means of reduction of the impact of organic radical reactions in the hot inlets by heterogeneous scavenging of e.g. $CH_3C(O)O_2$ and other RO_x species and also by reduction of the pressure and gas residence time in the inlets and cavities. These measures will reduce the total uncertainty in the measurements of PNs and ANs and extend the operational range of the instrument to higher NO_x regimes.

The Supplement related to this article is available online at doi:10.5194/amt-9-553-2016-supplement.

Acknowledgements. This work was carried out in part fulfilment of the PhD of J. Thieser, who thanks U. Platt for many helpful discussions and supervision of his thesis. We thank Christoph Groß for assistance in preparing the PAN sample. We thank Simone Stöppler and Thomas Elsinger of the "Hessischer Rundfunk" for mounting the DOAS retro-reflectors on the tower at the Großer Feldberg. We are grateful to Dupont for providing a sample of the FEP suspension used to coat the inlets and cavities.

The article processing charges for this open-access publication were covered by the Max Planck Society.

Edited by: A. Hofzumahaus

References

Atherton, C. S. and Penner, J. E.: The transformation of nitrogen oxides in the polluted troposphere, Tellus B, 40, 380–392, 1988.

Atkinson, R.: Gas-phase tropospheric chemistry of borganic compounds, J. Phys. Chem. Ref. Data, Monograph Nr., 21–216, 1994.

Atkinson, R. and Arey, J.: Atmospheric degradation of volatile organic compounds, Chem. Rev., 103, 4605–4638, doi:10.1021/cr0206420, 2003.

Atkinson, R., Baulch, D. L., Cox, R. A., Crowley, J. N., Hampson, R. F., Hynes, R. G., Jenkin, M. E., Rossi, M. J., and Troe, J.: Evaluated kinetic and photochemical data for atmospheric chemistry: Volume I – gas phase reactions of O_x, HO_x, NO_x and SO_x species, Atmos. Chem. Phys., 4, 1461–1738, doi:10.5194/acp-4-1461-2004, 2004.

Atkinson, R., Baulch, D. L., Cox, R. A., Crowley, J. N., Hampson, R. F., Hynes, R. G., Jenkin, M. E., Rossi, M. J., Troe, J., and IUPAC Subcommittee: Evaluated kinetic and photochemical data for atmospheric chemistry: Volume II – gas phase reactions of organic species, Atmos. Chem. Phys., 6, 3625–4055, doi:10.5194/acp-6-3625-2006, 2006.

Atlas, E.: Evidence for > C_3 alkyl nitrates in rural and remote atmosphere, Nature, 331, 426–428, 1988.

Ayers, J. D., Apodaca, R. L., Simpson, W. R., and Baer, D. S.: Off-axis cavity ringdown spectroscopy: application to atmospheric nitrate radical detection, Appl. Opt., 44, 7239–7242, 2005.

Baulch, D. L., Bowman, C. T., Cobos, C. J., Cox, R. A., Just, T., Kerr, J. A., Pilling, M. J., Stocker, D., Troe, J., Tsang, W., Walker, R. W., and Warnatz, J.: Evaluated kinetic data for combustion modeling: Supplement II, J. Phys. Chem. Ref. Data, 34, 757–1397, 2005.

Beaver, M. R., Clair, J. M. St., Paulot, F., Spencer, K. M., Crounse, J. D., LaFranchi, B. W., Min, K. E., Pusede, S. E., Wooldridge, P. J., Schade, G. W., Park, C., Cohen, R. C., and Wennberg, P. O.: Importance of biogenic precursors to the budget of organic nitrates: observations of multifunctional organic nitrates by CIMS and TD-LIF during BEARPEX 2009, Atmos. Chem. Phys., 12, 5773–5785, doi:10.5194/acp-12-5773-2012, 2012.

Berden, G., Peeters, R., and Meijer, G.: Cavity ring-down spectroscopy: Experimental schemes and applications, Int. Rev. Phys. Chem., 19, 565–607, 2000.

Brown, S. S.: Absorption spectroscopy in high-finesse cavities for atmospheric studies, Chem. Rev., 103, 5219–5238, 2003.

Brown, S. S. and Stutz, J.: Nighttime radical observations and chemistry, Chem. Soc. Rev., 41, 6405–6447, 2012.

Browne, E. C., Perring, A. E., Wooldridge, P. J., Apel, E., Hall, S. R., Huey, L. G., Mao, J., Spencer, K. M., Clair, J. M. St., Weinheimer, A. J., Wisthaler, A., and Cohen, R. C.: Global and regional effects of the photochemistry of $CH_3O_2NO_2$: evidence from ARCTAS, Atmos. Chem. Phys., 11, 4209–4219, doi:10.5194/acp-11-4209-2011, 2011.

Buhr, M. P., Parrish, D. D., Norton, R. B., Fehsenfeld, F. C., Sievers, R. E., and Roberts, J. M.: Contribution of Organic Nitrates to the Total Reactive Nitrogen Budget at a Rural Eastern U.S. Site, J. Geophys. Res., 95, 9809–9816, 1990.

Calvert, J. G. and Madronich, S.: Theoretical-study of the Initial Products of the Atmospheric Oxidation of Hydrocarbons, J. Geophys. Res.-Atmos., 92, 2211–2220, 1987.

Calvert, J. G., Atkinson, R., Kerr, J. A., Madronich, S., Moortgat, G. K., Wallington, T. J., and Yarwood, G.: The Mechanisms of Atmospheric Oxidation of the Alkenes, Oxford Univ. Press, New York, 2000.

Calvert, J. G., Atkinson, R., Becker, K. H., Seinfeld, J. H., Wallington, T. J., and Yarwood, G.: The mechanism of atmospheric oxidation of aromatic hydrocarbons, Oxford University Press, New York, 2002.

Carr, S. A., Baeza-Romero, M. T., Blitz, M. A., Pilling, M. J., Heard, D. E., and Seakins, P. W.: OH yields from the CH_3CO+O_2 reaction using an internal standard, Chem. Phys. Lett., 445, 108–112, 2007.

Carr, S. A., Glowacki, D. R., Liang, C.-H., Baeza-Romero, M. T., Blitz, M. A., Pilling, M. J., and Seakins, P. W.: Experimental and modeling studies of the pressure and temperature dependences of the kinetics and the OH yields in the acetyl + O_2 reaction, J. Phys. Chem. A, 115, 1069–1085, 2011.

Chen, S.-Y., and Lee, Y.-P.: Transient infrared absorption of t-$CH_3C(O)OO$, c-$CH_3C(O)OO$, and α-lactone recorded in gaseous reactions of CH_3CO and O_2, J. Chem. Phys., 132, 114303, doi:10.1063/1.3352315, 2010.

Crowley, J. N., Ammann, M., Cox, R. A., Hynes, R. G., Jenkin, M. E., Mellouki, A., Rossi, M. J., Troe, J., and Wallington, T. J.: Evaluated kinetic and photochemical data for atmospheric chemistry: Volume V – heterogeneous reactions on solid substrates, Atmos. Chem. Phys., 10, 9059–9223, doi:10.5194/acp-10-9059-2010, 2010a.

Crowley, J. N., Schuster, G., Pouvesle, N., Parchatka, U., Fischer, H., Bonn, B., Bingemer, H., and Lelieveld, J.: Nocturnal nitrogen oxides at a rural mountain-site in south-western Germany, Atmos. Chem. Phys., 10, 2795–2812, doi:10.5194/acp-10-2795-2010, 2010b.

Curtis, A. R., and Sweetenham, W. P.: Facsimile, Atomic Energy Research Establishment, Report R-12805, 1987.

Day, D. A., Wooldridge, P. J., Dillon, M. B., Thornton, J. A., and Cohen, R. C.: A thermal dissociation laser-induced fluorescence instrument for in situ detection of NO_2, peroxy nitrates, alkyl nitrates, and HNO_3, J. Geophys. Res.-Atmos., 107, doi:10.1029/2001jd000779, 2002.

Day, D. A., Dillon, M. B., Wooldridge, P. J., Thornton, J. A., Rosen, R. S., Wood, E. C., and Cohen, R. C.: On alkyl nitrates, O_3, and the "missing NOy", J. Geophys. Res.-Atmos., 108, 4501, doi:10.1029/2003jd003685, 2003.

Fahey, D. W., Hübler, G., Parrish, D. D., Williams, E. J., Norton, R. B., Ridley, B. A., Singh, H. B., Liu, S. C., and Fehsenfeld, F. C.: Reactive nitrogen species in the troposphere: measurements of NO, NO_2, HNO_3, particulate nitrate, peroxyacetyl nitrate (PAN), O_3, and total reactive odd Nitrogen (NO_y) at Niwot Ridge, Colorado, J. Geophys. Res., 91, 9781–9793, 1986.

Flocke, F. M., Weinheimer, A. J., Swanson, A. L., Roberts, J. M., Schmitt, R., and Shertz, S.: On the measurement of PANs by gas chromatography and electron capture detection, J. Atmos. Chem., 52, 19–43, 2005.

Fuchs, H., Dube, W. P., Lerner, B. M., Wagner, N. L., Williams, E. J., and Brown, S. S.: A sensitive and versatile detector for atmospheric NO_2 and NO_x Based on blue diode laser cavity ring-down spectroscopy, Env. Sci. Tech., 43, 7831–7836, doi:10.1021/es902067h, 2009.

Fuller, E. N., Schettle, P. D., and Giddings, J. C.: A new method for prediction of binary gas-phase diffusion coeffecients, Ind. Eng. Chem., 58, 19–27, 1966.

Groß, C. B. M., Dillon, T. J., and Crowley, J. N.: Pressure dependent OH yields in the reactions of CH_3CO and $HOCH_2CO$ with O_2, Phys. Chem. Chem. Phys., 16, 10990–10998, doi:10.1039/c4cp01108b, 2014.

Handisides, G. M.: The influence of peroxy radicals on ozone production, Fachbereich Geowissenschaften, Johann Wolfgang Goethe Universität, Frankfurt am Main, 115–132, 2001.

Hao, C. S., Shepson, P. B., Drummond, J. W., and Muthuramu, K.: Gas-chromatographic detector for selective and sensitive detection of atmospheric organic nitrates, Anal. Chem., 66, 3737–3743, 1994.

Hargrove, J., and Zhang, J.: Measurements of NO_x, acyl peroxynitrates, and NOy with automatic interference corrections using a NO_2 analyzer and gas phase titration, Rev. Sci. Instrum., 79, doi:10.1063/1.2908432, 2008.

Hosaynali Beygi, Z., Fischer, H., Harder, H. D., Martinez, M., Sander, R., Williams, J., Brookes, D. M., Monks, P. S., and Lelieveld, J.: Oxidation photochemistry in the Southern Atlantic boundary layer: unexpected deviations of photochemical steady state, Atmos. Chem. Phys., 11, 8497–8513, doi:10.5194/acp-11-8497-2011, 2011.

Huisman, A. J., Hottle, J. R., Galloway, M. M., DiGangi, J. P., Coens, K. L., Choi, W., Faloona, I. C., Gilman, J. B., Kuster, W. C., de Gouw, J., Bouvier-Brown, N. C., Goldstein, A. H., LaFranchi, B. W., Cohen, R. C., Wolfe, G. M., Thornton, J. A., Docherty, K. S., Farmer, D. K., Cubison, M. J., Jimenez, J. L., Mao, J., Brune, W. H., and Keutsch, F. N.: Photochemical modeling of glyoxal at a rural site: observations and analysis from BEARPEX 2007, Atmos. Chem. Phys., 11, 8883–8897, doi:10.5194/acp-11-8883-2011, 2011.

IUPAC: Task Group on Atmospheric Chemical Kinetic Data Evaluation, edited by: Ammann, M., Cox, R. A., Crowley, J. N., Jenkin, M. E., Mellouki, A., Rossi, M. J., Troe, J. and Wallington, T. J., available at: http://iupac.pole-ether.fr/index.html, last access: December 2015.

Kim, S., Huey, L. G., Stickel, R. E., Tanner, D. J., Crawford, J. H., Olson, J. R., Chen, G., Brune, W. H., Ren, X., Lesher, R., Wooldridge, P. J., Bertram, T. H., Perring, A., Cohen, R. C., Lefer, B. L., Shetter, R. E., Avery, M., Diskin, G., and Sokolik, I.: Measurement of HO_2NO_2 in the free troposphere during the intercontinental chemical transport experiment – North America 2004, J. Geophys. Res.-Atmos., 112, doi:10.1029/2006jd007676, 2007.

Kirchner, F., Mayer-Figge, A., Zabel, F., and Becker, K. H.: Thermal stability of peroxynitrates, Int. J. Chem. Kinet., 31, 127–144, 1999.

Kley, D. and McFarland, M.: Chemiluminescence detector for NO and NO_2, Atmos. Technol., 12, 63–69, 1980.

LaFranchi, B. W., Wolfe, G. M., Thornton, J. A., Harrold, S. A., Browne, E. C., Min, K. E., Wooldridge, P. J., Gilman, J. B., Kuster, W. C., Goldan, P. D., de Gouw, J. A., McKay, M., Goldstein, A. H., Ren, X., Mao, J., and Cohen, R. C.: Closing the peroxy acetyl nitrate budget: observations of acyl peroxy nitrates (PAN, PPN, and MPAN) during BEARPEX 2007, Atmos. Chem. Phys., 9, 7623–7641, doi:10.5194/acp-9-7623-2009, 2009.

Lee, J., Chen, C.-J., and Bozzelli, J. W.: Thermochemical and kinetic analysis of the acetyl radical $(CH_3CO) + O_2$ Reaction System, J. Phys. Chem. A, 106, 7155–7170, doi:10.1021/jp014443g, 2002.

Lee, L., Wooldridge, P. J., Gilman, J. B., Warneke, C., de Gouw, J., and Cohen, R. C.: Low temperatures enhance organic nitrate formation: evidence from observations in the 2012 Uintah Basin Winter Ozone Study, Atmos. Chem. Phys., 14, 12441–12454, doi:10.5194/acp-14-12441-2014, 2014.

Lee, Y.-N., Zhou, X.-L., and Hallock, K.: Atmospheric carbonyl compounds at a rural southeastern United States site, J. Geophys. Res., 100, 25933–25944, 1995.

Li, J., Reiffs, A., Parchatka, U., and Fischer, H.: In situ measurements of atmospheric CO and its correlation with NOx and O_3 at a rural mountain site, Metrol. Meas. Sys. , XXII, 25–38, 2015.

Meller, R., Raber, W., Crowley, J. N., Jenkin, M. E., and Moortgat, G. K.: The UV-visible absorption spectrum of methylglyoxal, J. Photochem. Photobiol. A-Chem., 62, 163–171, 1991.

Merten, A., Tschritter, J., and Platt, U.: Design of differential optical absorption spectroscopy long-path telescopes based on fiber optics, Appl. Opt., 50, 738–754, 2011.

Mielke, L. H. and Osthoff, H. D.: On quantitative measurements of peroxycarboxylic nitric anhydride mixing ratios by thermal dissociation chemical ionization mass spectrometry, Int. J. Mass Spectrom., 310, 1–9, doi:10.1016/j.ijms.2011.10.005, 2012.

Mielke, L. H., Stutz, J., Tsai, C., Hurlock, S. C., Roberts, J. M., Veres, P. R., Froyd, K. D., Hayes, P. L., Cubison, M. J., Jimenez, J. L., Washenfelder, R. A., Young, C. J., Gilman, J. B., de Gouw, J. A., Flynn, J. H., Grossberg, N., Lefer, B. L., Liu, J., Weber, R. J., and Osthoff, H. D.: Heterogeneous formation of nitryl chloride and its role as a nocturnal NO_x reservoir species during CalNex-LA 2010, J. Geophys. Res.-Atmos., 118, 10638–10652, doi:10.1002/jgrd.50783, 2013.

Murphy, J. G., Thornton, J. A., Wooldridge, P. J., Day, D. A., Rosen, R. S., Cantrell, C., Shetter, R. E., Lefer, B., and Cohen, R. C.: Measurements of the sum of HO_2NO_2 and $CH_3O_2NO_2$ in the remote troposphere, Atmos. Chem. Phys., 4, 377–384, doi:10.5194/acp-4-377-2004, 2004.

Nault, B. A., Garland, C., Pusede, S. E., Wooldridge, P. J., Ullmann, K., Hall, S. R., and Cohen, R. C.: Measurements of $CH_3O_2NO_2$ in the upper troposphere, Atmos. Meas. Tech., 8, 987–997, doi:10.5194/amt-8-987-2015, 2015.

Neuman, J. A., Huey, L. G., Ryerson, T. B., and Fahey, D. W.: Study of inlet materials for sampling atmospheric nitric acid, Env. Sci. Tech., 33, 1133–1136, 1999.

Osthoff, H. D., Roberts, J. M., Ravishankara, A. R., Williams, E. J., Lerner, B. M., Sommariva, R., Bates, T. S., Coffman, D., Quinn, P. K., Dibb, J. E., Stark, H., Burkholder, J. B., Talukdar, R. K., Meagher, J., Fehsenfeld, F. C., and Brown, S. S.: High levels of nitryl chloride in the polluted subtropical marine boundary layer, Nat. Geosci., 1, 324–328, 2008.

Papadimitriou, V. C., Karafas, E. S., Gierczak, T., and Burkholder, J. B.: $CH_3CO + O_2 + M$ (M = He, N_2) reaction rate coefficient measurements and implications for the OH radical product yield, J. Phys. Chem. A, 119, 7481–7497, doi:10.1021/acs.jpca.5b00762, 2015.

Parrish, D. D. and Buhr, M. P.: Measurement challenges of nitrogen species in the atmosphere, Adv. Chem., 232, 243–273, doi:10.1021/ba-1993-0232.ch009, 1993.

Paul, D., Furgeson, A., and Osthoff, H. D.: Measurements of total peroxy and alkyl nitrate abundances in laboratory-generated gas samples by thermal dissociation cavity ring-down spectroscopy, Rev. Sci. Instrum., 80, Art. 114101, doi:10.1063/1.3258204, 2009.

Paul, D. and Osthoff, H. D.: Absolute Measurements of Total Peroxy Nitrate Mixing Ratios by Thermal Dissociation Blue Diode Laser Cavity Ring-Down Spectroscopy, Anal. Chem., 82, 6695–6703, doi:10.1021/ac101441z, 2010.

Perring, A. E., Pusede, S. E., and Cohen, R. C.: An observational perspective on the atmospheric impacts of alkyl and multifunctional nitrates on ozone and secondary organic aerosol, Chem. Rev., 113, 5848–5870, doi:10.1021/cr300520x, 2013.

Peukert, S. L., Sivaramakrishnan, R., and Michael, J. V.: High temperature shock tube studies on the thermal decomposition of O_3 and the reaction of dimethyl carbonate with O-Atoms, J. Phys. Chem. A, 117, 3729–3738, doi:10.1021/jp400613p, 2013.

Phillips, G. J., Tang, M. J., Thieser, J., Brickwedde, B., Schuster, G., Bohn, B., Lelieveld, J., and Crowley, J. N.: Significant concentrations of nitryl chloride observed in rural continental Europe associated with the influence of sea salt chloride and anthropogenic emissions, Geophys. Res. Lett., 39, L10811, doi:10.1029/2012GL051912, 2012.

Phillips, G. J., Pouvesle, N., Thieser, J., Schuster, G., Axinte, R., Fischer, H., Williams, J., Lelieveld, J., and Crowley, J. N.: Peroxyacetyl nitrate (PAN) and peroxyacetic acid (PAA) measurements by iodide chemical ionisation mass spectrometry: first analysis of results in the boreal forest and implications for the measurement of PAN fluxes, Atmos. Chem. Phys., 13, 1129–1139, doi:10.5194/acp-13-1129-2013, 2013.

Pöhler, D., Vogel, L., Friess, U., and Platt, U.: Observation of halogen species in the Amundsen Gulf, Arctic, by active long-path differential optical absorption spectroscopy, Proc. Natl. Acad. Sci. USA, 107, 6582–6587, doi:10.1073/pnas.0912231107, 2010.

Ridley, B. A., Shetter, J. D., Walega, J. G., Madronich, S., Elsworth, C. M., Grahek, F. E., Fehsenfeld, F. C., Norton, R. B., Parrish, D. D., Hübler, G., Buhr, M., Williams, E. J., Allwine, E. J., and Westberg, H. H.: The Behavior of Some Organic Nitrates at Boulder and Niwot Ridge, Colorado, J. Geophys. Res., 95, 13949–13961, 1990.

Roberts, J. M.: The atmospheric chemistry of organic nitrates, Atmos. Environ., Part A, 24, 243–287, doi:10.1016/0960-1686(90)90108-y, 1990.

Roberts, J. M., Jobson, B. T., Kuster, W., Goldan, P., Murphy, P., Williams, E., Frost, G., Riemer, D., Apel, E., Stroud, C., Wiedinmyer, C., and Fehsenfeld, F.: An examination of the chemistry of peroxycarboxylic nitric anhydrides and related volatile organic compounds during Texas Air Quality Study 2000 using ground-based measurements, J. Geophys. Res.-Atmos., 108, 4495, doi:10.1029/2003jd003383, 2003.

Roiger, A., Aufmhoff, H., Stock, P., Arnold, F., and Schlager, H.: An aircraft-borne chemical ionization – ion trap mass spectrometer (CI-ITMS) for fast PAN and PPN measurements, Atmos. Meas. Tech., 4, 173–188, doi:10.5194/amt-4-173-2011, 2011.

Rosen, R. S., Wood, E. C., Wooldridge, P. J., Thornton, J. A., Day, D. A., Kuster, W., Williams, E. J., Jobson, B. T., and Cohen, R. C.: Observations of total alkyl nitrates during Texas Air Quality Study 2000: Implications for O_3 and alkyl nitrate photochemistry, J. Geophys. Res.-Atmos., 109, D07303, doi:10.1029/2003jd004227, 2004.

Rothman, L. S., Gordon, I. E., Babikov, Y., Barbe, A., Benner, D. C., Bernath, P. F., Birk, M., Bizzocchi, L., Boudon, V., Brown, L. R., Campargue, A., Chance, K., Cohen, E. A., Coudert, L. H., Devi, V. M., Drouin, B. J., Fayt, A., Flaud, J. M., Gamache, R. R., Harrison, J. J., Hartmann, J. M., Hill, C., Hodges, J. T., Jacquemart, D., Jolly, A., Lamouroux, J., Le Roy, R. J., Li, G., Long, D. A., Lyulin, O. M., Mackie, C. J., Massie, S. T., Mikhailenko, S., Mueller, H. S. P., Naumenko, O. V., Nikitin, A. V., Orphal, J., Perevalov, V., Perrin, A., Polovtseva, E. R., Richard, C., Smith, M. A. H., Starikova, E., Sung, K., Tashkun, S., Tennyson, J., Toon, G. C., Tyuterev, V. G., and Wagner, G.: The HITRAN2012 molecular spectroscopic database, J. Quant. Spectrosc. R., 130, 4–50, doi:10.1016/j.jqsrt.2013.07.002, 2013.

Ryerson, T. B., Williams, E. J., and Fehsenfeld, F. C.: An efficient photolysis system for fast-response NO_2 measurements, J. Geophys. Res.-Atmos., 105, 26447–26461, doi:10.1029/2000jd900389, 2000.

Schneider, M. and Ballschmiter, K.: C3–C14 alkyl nitrates in remote South Atlantic air, Chemosphere, 38, 233–244, 1999.

Schuster, G., Labazan, I., and Crowley, J. N.: A cavity ring down/cavity enhanced absorption device for measurement of ambient NO_3 and N_2O_5, Atmos. Meas. Tech., 2, 1–13, doi:10.5194/amt-2-1-2009, 2009.

Singh, H. B. and Hanst, P. L.: Peroxyacetyl nitrate (PAN) in the unpolluted atmosphere: An important reservoir for nitrogen oxides, Geophys. Res. Lett., 8, 941–944, 1981.

Singh, H. B., Herlth, D., Kolyer, R., Salas, L., Bradshaw, J. D., Sandholm, S. T., Davis, D. D., Crawford, J., Kondo, Y., Koike, M., Talbot, R., Gregory, G. L., Sachse, G. W., Browell, E., Blake, D. R., Rowland, F. S., Newell, R., Merrill, J., Heikes, B., Liu, S. C., Crutzen, P. J., and Kanakidou, M.: Reactive nitrogen and ozone over the western Pacific: Distribution, partitioning, and sources, J. Geophys. Res., 101, 1793–1808, 1996.

Slusher, D. L., Huey, L. G., Tanner, D. J., Chen, G., Davis, D. D., Buhr, M., Nowak, J. B., Eisele, F. L., Kosciuch, E., Mauldin, R. L., Lefer, B. L., Shetter, R. E., and Dibb, J. E.: Measurements of pernitric acid at the South Pole during ISCAT 2000, Geophys. Res. Lett., 29, 2011, doi:10.1029/2002gl015703, 2002.

Slusher, D. L., Huey, L. G., Tanner, D. J., Flocke, F. M., and Roberts, J. M.: A thermal dissociation-chemical ionization mass spectrometry (TD-CIMS) technique for the simultaneous measurement of peroxyacyl nitrates and dinitrogen pentoxide, J. Geophys. Res.-Atmos., 109, D19315, doi:10.1029/2004JD004670, 2004.

Suitters, M.: Long Path DOAS: The PARADE campaign, mode mixing and light source comparisons, Master Thesis, Institut for Environmental Physics, Heidelberg, 2012.

Talukdar, R. K., Burkholder, J. B., Schmoltner, A. M., Roberts, J. M., Wilson, R. R., and Ravishankara, A. R.: Investigation of the loss processes for peroxyacetyl nitrate in the atmosphere: UV photolysis and reaction with OH, J. Geophys. Res.-Atmos., 100, 14163–14173, doi:10.1029/95jd00545, 1995.

Talukdar, R. K., Herndon, S. C., Burkholder, J. B., Roberts, J. M., and Ravishankara, A. R.: Atmospheric fate of several alkyl nitrates .1. Rate coefficients of the reactions alkyl nitrates with isotopically labelled hydroxyl radicals, J. Chem. Soc. Faraday T., 93, 2787–2796, 1997.

Tang, M. J., Thieser, J., Schuster, G., and Crowley, J. N.: Kinetics and mechanism of the heterogeneous reaction of N_2O_5 with mineral dust particles, Phys. Chem. Chem. Phys, 14, 8551–8561, 2012.

Thaler, R. D., Mielke, L. H., and Osthoff, H. D.: Quantification of nitryl chloride at part per trillion mixing ratios by thermal dissociation cavity ring-down spectroscopy, Anal. Chem., 83, 2761–2766, doi:10.1021/ac200055z, 2011.

Thornton, J. A., Kercher, J. P., Riedel, T. P., Wagner, N. L., Cozic, J., Holloway, J. S., Dube, W. P., Wolfe, G. M., Quinn, P. K., Middlebrook, A. M., Alexander, B., and Brown, S. S.: A large atomic chlorine source inferred from mid-continental reactive nitrogen chemistry, Nature, 464, 271–274, doi:10.1038/nature08905, 2010.

Trainer, M., Buhr, M. P., Curran, C. M., Fehsenfeld, F. C., Hsie, E. Y., Liu, S. C., Norton, R. B., Parrish, D. D., Williams, E. J., Gandrud, B. W., Ridley, B. A., Shetter, J. D., Allwine, E. J., and Westberg, H. H.: Observations and Modeling of the Reactive Nitrogen Photochemistry at a Rural Site, J. Geophys. Res., 96, 3045–3063, 1991.

Tyndall, G. S., Staffelbach, T. A., Orlando, J. J., and Calvert, J. G.: Rate coefficients for the reactions of OH radicals with methylglyoxal and acetaldehyde, Int. J. Chem. Kinet., 27, 1009–1020, 1995.

Voigt, S., Orphal, J., and Burrows, J. P.: The temperature and pressure dependence of the absorption cross-sections of NO_2 in the 250–800 nm region measured by Fourier-transform spectroscopy, J. Photochem. Photobiol. A-Chem., 149, 1–7, doi:10.1016/s1010-6030(01)00650-5, 2002.

Volkamer, R., Molina, L. T., Molina, M. J., Shirley, T., and Brune, W. H.: DOAS measurement of glyoxal as an indicator for fast VOC chemistry in urban air, Geophys. Res. Lett., 32, L08806, doi:10.1029/2005gl022616, 2005a.

Volkamer, R., Spietz, P., Burrows, J., and Platt, U.: High-resolution absorption cross-section of glyoxal in the UV-vis and IR spectral ranges, J. Photochem. Photobiol. A-Chem., 172, 35–46, doi:10.1016/j.jphotochem.2004.11.011, 2005b.

Wagner, N. L., Riedel, T. P., Roberts, J. M., Thornton, J. A., Angevine, W. M., Williams, E. J., Lerner, B. M., Vlasenko, A., Li, S. M., Dube, W. P., Coffman, D. J., Bon, D. M., de Gouw, J. A., Kuster, W. C., Gilman, J. B., and Brown, S. S.: The sea breeze/land breeze circulation in Los Angeles and its influence on nitryl chloride production in this region, J. Geophys. Res.-Atmos., 117, D00V24, doi:10.1029/2012jd017810, 2012.

Warneck, P. and Zerbach, T.: Synthesis of peroxyacetyl nitrate in air by acetone photolysis, Env. Sci. Tech., 26, 74–79, 1992.

Wild, R. J., Edwards, P. M., Dube, W. P., Baumann, K., Edgerton, E. S., Quinn, P. K., Roberts, J. M., Rollins, A. W., Veres, P. R., Warneke, C., Williams, E. J., Yuan, B., and Brown, S. S.: A measurement of total reactive nitrogen, NOy, together with NO_2, NO, and O_3 via cavity ring-down spectroscopy, Env. Sci. Tech., 48, 9609–9615, doi:10.1021/es501896w, 2014.

Williams, J., Roberts, J. M., Fehsenfeld, F. C., Bertman, S. B., Buhr, M. P., Goldan, P. D., Hubler, G., Kuster, W. C., Ryerson, T. B., Trainer, M., and Young, V.: Regional ozone from biogenic hydrocarbons deduced from airborne measurements of PAN, PPN, and MPAN, Geophys. Res. Lett., 24, 1099–1102, 1997.

Wolfe, G. M., Thornton, J. A., Yatavelli, R. L. N., McKay, M., Goldstein, A. H., LaFranchi, B., Min, K.-E., and Cohen, R. C.: Eddy covariance fluxes of acyl peroxy nitrates (PAN, PPN and MPAN) above a Ponderosa pine forest, Atmos. Chem. Phys., 9, 615–634, doi:10.5194/acp-9-615-2009, 2009.

Wooldridge, P. J., Perring, A. E., Bertram, T. H., Flocke, F. M., Roberts, J. M., Singh, H. B., Huey, L. G., Thornton, J. A., Wolfe, G. M., Murphy, J. G., Fry, J. L., Rollins, A. W., LaFranchi, B. W., and Cohen, R. C.: Total Peroxy Nitrates (SPNs) in the atmosphere: the Thermal Dissociation-Laser Induced Fluorescence (TD-LIF) technique and comparisons to speciated PAN measurements, Atmos. Meas. Tech., 3, 593–607, doi:10.5194/amt-3-593-2010, 2010.

Zheng, W., Flocke, F. M., Tyndall, G. S., Swanson, A., Orlando, J. J., Roberts, J. M., Huey, L. G., and Tanner, D. J.: Characterization of a thermal decomposition chemical ionization mass spectrometer for the measurement of peroxy acyl nitrates (PANs) in the atmosphere, Atmos. Chem. Phys., 11, 6529–6547, doi:10.5194/acp-11-6529-2011, 2011.